Journal of Peridynamics and Nonlocal Modeling (2025) 7:0
https://doi.org/10.1007/s42102-024-00125-z

RESEARCH

Nonlocal Nernst-Planck-Poisson System for Modeling Electrochemical Corrosion in Biodegradable Magnesium Implants

Alexander Hermann[1] · **Arman Shojaei**[1] · **Daniel Höche**[2] · **Siavash Jafarzadeh**[3] · **Florin Bobaru**[4] · **Christian J. Cyron**[1,5]

Received: 15 July 2024 / Accepted: 21 August 2024

Abstract

This paper provides a comprehensive derivation and application of the nonlocal Nernst-Planck-Poisson (NNPP) system for accurate modeling of electrochemical corrosion with a focus on the biodegradation of magnesium-based implant materials under physiological conditions. The NNPP system extends and generalizes the peridynamic bi-material corrosion model by considering the transport of multiple ionic species due to electromigration. As in the peridynamic corrosion model, the NNPP system naturally accounts for moving boundaries due to the electrochemical dissolution of solid metallic materials in a liquid electrolyte as part of the dissolution process. In addition, we use the concept of a diffusive corrosion layer, which serves as an interface for constitutive corrosion modeling and provides an accurate representation of the kinetics with respect to the corrosion system under consideration. Through the NNPP model, we propose a corrosion modeling approach that incorporates diffusion, electromigration and reaction conditions in a single nonlocal framework. The validity of the NNPP-based corrosion model is illustrated by numerical simulations, including a one-dimensional example of pencil electrode corrosion and a three-dimensional simulation of a Mg-10Gd alloy bone implant screw decomposing in simulated body fluid. The numerical simulations correctly reproduce the corrosion patterns in agreement with macroscopic experimental corrosion data. Using numerical models of corrosion based on the NNPP system, a nonlocal approach to corrosion analysis is proposed, which reduces the gap between experimental observations and computational predictions, particularly in the development of biodegradable implant materials.

✉ Alexander Hermann
alexander.hermann@hereon.de

[1] Institute of Material Systems Modeling, Helmholtz-Zentrum Hereon, Max-Planck-Str. 1, 21502 , Geesthacht, Germany

[2] Institute of Surface Science, Helmholtz-Zentrum Hereon, Max-Planck-Str. 1, 21502, Geesthacht, Germany

[3] Department of Mathematics, Lehigh University, Bethlehem, PA 18015, USA

[4] Department of Mechanical & Materials Engineering, University of Nebraska-Lincoln, Lincoln, NE 68588-0526, USA

[5] Institute for Continuum and Material Mechanics, Hamburg University of Technology, Eissendorfer Strasse 42, 21073 Hamburg, Germany

Keywords Nernst-Planck-Poisson system · Corrosion modeling · Electromigration · Peridynamics · Implant materials · Biodegradation

1 Introduction

In recent times, there has been an increasing growth in the development of numerical models for simulating electrochemical corrosion phenomena. The main difficulty encountered by these models is the accurate representation of the moving boundary between the solid metallic material and the liquid electrolyte, which moves due to the electrochemical dissolution of the metallic phase. In addition, the rigorous description of the electrical double layer at the interface and the representation of the corrosion kinetics for a given composition of the metallic material and the surrounding electrolyte medium is a very challenging task. Numerical models such as these are of particular interest for simulating the degradation of magnesium (Mg)-based alloys in physiological environments. Currently, these alloys are the subject of active research and have already found application in the development of biodegradable materials for implants [28, 44, 48, 64, 69]. Due to their biodegradability, biocompatibility, and ability to promote bone growth, Mg-based alloys are widely regarded as new and promising materials for implants [2, 38, 42]. Numerous experimental studies have examined the degradation of Mg alloys both *in vitro*, using different cell culture media to mimic physiological conditions, and *in vivo* in various animal models [23, 49, 68]. Despite these efforts, discrepancies between in vitro and in vivo results persist. The use of computational models as digital twins may bridge this gap and allow predictions to be made based on *in vivo* data and thus potentially reduce the resources required for experimental studies in the development of new implant materials [1, 56, 69].

A wide range of computational methods have been used to study corrosion problems, which generally fall into two categories: Sharp interface models that trace moving corrosion surfaces, such as the finite element method (FEM), the arbitrary Lagrangian-Eulerian method (ALE) and the level set method (LSM), and diffuse interface models, such as phase field (PF) approaches [5, 12, 24, 25, 37, 43]. Sharp interface models mainly use FEM models to solve the electrochemical transport equations in the computational domain. These models are generally non-autonomous and require additional methods to determine the interface velocity and corrosion surface tracking, which introduces additional complexities for their practical application. Nevertheless, sharp interface models have been successfully used in modeling the biodegradation of implant materials using effective diffusion modeling techniques and have been validated against the macroscopic properties of metallic samples in 3D spaces [21].

The PF approach, exemplified for autonomous models, has proven to be particularly suitable for corrosion problems. It is characterized by the use of an auxiliary field variable to continuously describe the corrosion interface between the solid metallic and liquid electrolyte phases, going from 0 values to 1 values, respectively [47, 53]. In contrast to models that explicitly track the evolution of the corrosion interface, PF models provide a continuous description of the interface, which avoids sharp mathematical discontinuities at the corrosion interface and autonomously captures the evolution of the corrosion surface without the need to manually determine the interface velocity. Consequently, PF methods can adeptly capture topological degradation in up to 3D spaces. The versatility of the PF method has led to wide research and application in diverse corrosion phenomena such as homogeneous corrosion, stress-corrosion, precipitation formation, and localization [6, 7, 35, 43, 46]. Recently, it has also been applied to the study of biocompatible alloy degradation in physiological environments. This includes modeling multi-ionic mass transport due to corrosion, precipitation layer formation and dissolution, and the evolution of mechanical damage in 3D implants [37, 55]. In spite of the significant progress made in its application to bio-corrosion of implant materials, PF modeling suffers from several computational issues. The underlying coupled nonlinear partial differential equations, necessary for accurately simulating phase transitions, electric field variations, mass transfer, and mechanical damage, increase the computational intensity, especially for 3D problems. In addition, PF models based on diffusion-reaction systems use given functional changes at the interface of corrosion rearrangement, which may not mirror the real electrochemical processes directly [67].

Recent theoretical and computational developments have drawn attention to the applicability of nonlocal and peridynamic (PD) models as effective tools for modeling problems in ion transport and electrochemical corrosion [4, 27, 65]. The underlying PD theory established in [62] has since been extended to solve a variety of problems in both solid and fluid mechanics with notable success [8, 17, 34, 50, 54, 59, 63]. The work in [9, 10] presents a transient peridynamic heat model that conceptualizes nonlocal coupling interactions as channels between *heat buckets*. This novel view conceptualizes heat transfer to a material point through tube-like interactions within a certain finite radius − called the peridynamic *horizon*. The peridynamic formulation naturally incorporates evolving discontinuities in the model, thereby preserving the validity of the integro-differential equations even at sharp discontinuities. Later extensions of this work successfully adapted the model for nonlocal diffusion-advection-reaction systems in 3D contexts [65].

In [13], the first PD model has been proposed to simulate pitting corrosion in salt water. This model is characterized by its ability to simulate subsurface corrosion damage, a common phenomenon in various corrosion processes when the surface is wetted, without the need to calculate the interface velocity or explicitly track the corrosion front. In addition, this model provides a damage field that can be used for subsequent mechanical damage analysis [31]. Further developments have extended the scope of this approach to include complex phenomena such as passivation, salt layer formation and intergranular corrosion, stress corrosion and stress corrosion cracking (SCC), etc. [15, 29, 30, 32, 33].

While PD corrosion models have shown promising potential in numerical corrosion modeling, the rigorous derivation of a nonlocal ionic electromigration system remains unaddressed. Our study aims to fill this gap. In [39], the classical Nernst-Planck electromigration model was first extended to a nonlocal context and various electroneutrality constraints were evaluated in one dimensional (1D) space. This work introduced a nonlocal version of the Nernst-Planck equations as well as a nonlocal electroneutrality constraint based on the electrostatic Poisson equation, which is typically derived from Maxwell's equations. We follow this approach by extending these equations to 3D spaces and demonstrate their convergence in the nonlocal-to-local limit to the classical Nernst-Planck-Poisson system. The original Nernst-Planck model accounts for ion migration, including Fick diffusion, as well as an additional term for electromigration of charged ions due to the influence of the electrostatic potential distribution [20]. The adaptation in [39] introduces a new method to determine this migration term nonlocally, by averaging the ion concentrations between two material points within a given horizon of interaction. Our results confirm this approach, but point out the need for a correction: a factor of 2 is required to ensure precise convergence to the classical equations in the nonlocal-to-local limit.

This paper is organized as follows: Section 2 provides a detailed derivation of the nonlocal Nernst-Planck-Poisson (NNPP) system for electromigration, starting from the scenario of two parallel infinite planes with different values of concentration and electrostatic potential. In Section 3, we study the NNPP system in its general form and illustrate its convergence to the classical Nernst-Planck-Poisson system in the limit of vanishing nonlocal interactions via a

Taylor series expansion for the governing field variables. Section 4 discusses how the NNPP equations can be applied to PD corrosion modeling, including the integration of constitutive models in the liquid and solid phases as well as the diffusive corrosion layer at the interface. In Section 5, we present a semi-implicit, discrete formulation of the NNPP governing equations along with a numerical solution strategy employing the Newton-Raphson iterative scheme. In Sections 6 and 7, we present numerical examples of PD corrosion models. In the first section, a one-dimensional model of pencil electrode corrosion in salt water is presented, simulating steel alloy corrosion and hydroxide layer formation with standard Butler-Volmer corrosion kinetics. The latter section deals with a complex three-dimensional corrosion system studying the degradation of a Mg alloy with 10% gadolinium (Mg-10Gd) *in vitro*, using simulated body fluid (SBF) to simulate physiological conditions over an eight-week immersion period. The article concludes with Section 8 that summarizes the results and contributions of the study.

2 Nonlocal Formulation of Electromigration

In this section, we provide the derivation of the NNPP system. This derivation extends the PD approach to transient heat conduction outlined in [9, 10] to account for ionic electromigration. We begin by considering two points, $\mathbf{x}$ and $\hat{\mathbf{x}}$, positioned on two parallel planes separated by distance d, with these planes maintaining different concentration values, specifically $c(\hat{\mathbf{x}}) > c(\mathbf{x})$, as illustrated schematically in Fig. 1. The concentration transfer between these planes across a surface area S is described by

$$S(\hat{J}_d - J_d) = SD\frac{c(\hat{\mathbf{x}}, t) - c(\mathbf{x}, t)}{d}, \tag{1}$$

where $\hat{J}_d$ and J_d represent the diffusion-related fluxes per unit time and area at $\hat{\mathbf{x}}$ and $\mathbf{x}$, respectively, and D denotes the medium's diffusion coefficient. Furthermore, we introduce the electromigration-related flow densities J_e and $\hat{J}_e$, i.e., the number of ions crossing a surface area perpendicular to their direction of motion at the respective points as

$$\begin{aligned} \hat{J}_e &= \hat{v}c(\hat{\mathbf{x}}, t), \\ J_e &= vc(\mathbf{x}, t), \end{aligned} \tag{2}$$

where $\hat{v}$ and v are the velocities at the planes' respective spatial positions. Considering mobility μ and the force F_e acting under electrical influence, the velocities are given by

$$\begin{aligned} v &= \mu F_e, \\ \hat{v} &= \mu \hat{F}_e. \end{aligned} \tag{3}$$

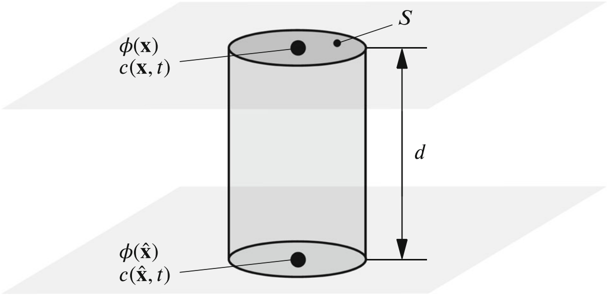

Fig. 1 Concentration transfer in a tube bounded by two parallel planes with distinct concentration and electrostatic potential values

Assuming the planes are at different electric potentials, $\phi(\hat{\mathbf{x}})$ and $\phi(\mathbf{x})$, the forces exerted by a homogeneous electric field, denoted as F_e and $\hat{F}_e$, due to the potential difference over distance d, can be expressed as

$$\begin{aligned} F_e &= -zF\frac{\phi(\hat{\mathbf{x}}) - \phi(\mathbf{x})}{d}, \\ \hat{F}_e &= -zF\frac{\phi(\mathbf{x}) - \phi(\hat{\mathbf{x}})}{d}. \end{aligned} \tag{4}$$

Here, z represents the valence of the charge and F is Faraday's constant. We now introduce c_a as the average concentration within a cylindrical volume defined by a cross-sectional area S and length d between points $\hat{\mathbf{x}}$ and $\mathbf{x}$. The rate of change in concentration, c_a, is given by

$$d\frac{\partial c_a}{\partial t} \approx \hat{J} - J = D\frac{c(\hat{\mathbf{x}}, t) - c(\mathbf{x}, t)}{d} + \mu z F\frac{\phi(\hat{\mathbf{x}}) - \phi(\mathbf{x})}{d}\left(c(\hat{\mathbf{x}}, t) + c(\mathbf{x}, t)\right), \tag{5}$$

where the total fluxes, $\hat{J}$ and J, through surfaces S at $\hat{\mathbf{x}}$ and $\mathbf{x}$, respectively, are composed of

$$\begin{aligned} \hat{J} &= \hat{J}_d + \hat{J}_e, \\ J &= J_d + J_e. \end{aligned} \tag{6}$$

By employing the Einstein relation, we relate the electrical mobility μ to the medium's diffusion coefficient D as

$$\mu = \frac{D}{RT}, \tag{7}$$

where R denotes the gas constant and T the temperature. In analogy to the approach taken for the PD transient heat equation in [9], one could proceed analyzing the behavior as the separation distance d between the points $\hat{\mathbf{x}}$ and $\mathbf{x}$ approaches zero. Under this condition, Eq. 5 transitions to a spatial gradient representation, thereby recovering the classical Nernst-Planck formulation. Extending the methodology outlined in [9] to the nonlocal modeling of electromigration, we first consider a collection of material points distributed across a 3D space Ω, where each point is connected to its neighbors within a spherical vicinity characterized by a radius δ, i.e., the PD horizon. Let $\mathbf{e}$ be the unit vector along the bond vector between the points $\hat{\mathbf{x}}$ and $\mathbf{x}$. It is posited that electromigration occurs independently along the bonds within this defined neighborhood, treating the bonds as insulated conduits. For a given point $\mathbf{x}$ within Ω, the 1D nonlocal Nernst-Planck equation for a singular bond $(\hat{\mathbf{x}}, \mathbf{x})$ oriented along $\mathbf{e}$ can be formulated as

$$(\hat{\mathbf{x}} - \mathbf{x}) \cdot \mathbf{e}\frac{\partial c_a(\hat{\mathbf{x}}, \mathbf{x}, t)}{\partial t} = D\left(\frac{c(\hat{\mathbf{x}}, t) - c(\mathbf{x}, t)}{(\hat{\mathbf{x}} - \mathbf{x}) \cdot \mathbf{e}} + \frac{zF}{RT}\frac{\phi(\hat{\mathbf{x}}) - \phi(\mathbf{x})}{(\hat{\mathbf{x}} - \mathbf{x}) \cdot \mathbf{e}}\left(c(\hat{\mathbf{x}}, t) + c(\mathbf{x}, t)\right)\right), \tag{8}$$

where $c_a(\hat{\mathbf{x}}, \mathbf{x}, t)$ denotes the average concentration along the bond $(\hat{\mathbf{x}}, \mathbf{x})$. Assuming a constant and isotropic diffusion coefficient D, we divide both sides of Eq. 8 by the finite distance $(\hat{\mathbf{x}} - \mathbf{x}) \cdot \mathbf{e}$ and integrate over the spherical neighborhood $\mathcal{H}_{\mathbf{x}}$ with radius δ yielding

$$\int_{\mathcal{H}_{\mathbf{x}}} \frac{\partial c_a(\hat{\mathbf{x}}, \mathbf{x}, t)}{\partial t}\mathrm{d}V_{\hat{\mathbf{x}}} = \int_{\mathcal{H}_{\mathbf{x}}} D\left(\frac{c(\hat{\mathbf{x}}, t) - c(\mathbf{x}, t)}{\|\hat{\mathbf{x}} - \mathbf{x}\|^2} + \frac{zF}{RT}\frac{\phi(\hat{\mathbf{x}}) - \phi(\mathbf{x})}{\|\hat{\mathbf{x}} - \mathbf{x}\|^2}\left(c(\hat{\mathbf{x}}, t) + c(\mathbf{x}, t)\right)\right)\mathrm{d}V_{\hat{\mathbf{x}}}. \tag{9}$$

We postulate that the rate of change in concentration at a point $\mathbf{x}$ over time, $c(\mathbf{x}, t)$, correlates with the rate of change in the average concentration, $c_a(\hat{\mathbf{x}}, \mathbf{x}, t)$, for all connections to $\mathbf{x}$ within its immediate vicinity, which is expressed as

$$\int_{\mathcal{H}_{\mathbf{x}}} \frac{\partial c_a(\hat{\mathbf{x}}, \mathbf{x}, t)}{\partial t}\mathrm{d}V_{\hat{\mathbf{x}}} = \frac{\partial c(\mathbf{x}, t)}{\partial t}V_{\mathcal{H}_{\mathbf{x}}}, \tag{10}$$

where $V_{\mathcal{H}_\mathbf{x}}$ represents the volume over the neighborhood of $\mathbf{x}$. Consequently, the integral form in Eq. 9 simplifies to

$$\frac{\partial c(\mathbf{x},t)}{\partial t} = \int_{\mathcal{H}_\mathbf{x}} \kappa \left(\frac{c(\hat{\mathbf{x}},t) - c(\mathbf{x},t)}{\|\hat{\mathbf{x}} - \mathbf{x}\|^2} + \frac{zF}{RT} \frac{\phi(\hat{\mathbf{x}}) - \phi(\mathbf{x})}{\|\hat{\mathbf{x}} - \mathbf{x}\|^2} \big(c(\hat{\mathbf{x}},t) + c(\mathbf{x},t) \big) \right) \mathrm{d}V_{\hat{\mathbf{x}}}, \quad (11)$$

with $\kappa = D/V_{\mathcal{H}_\mathbf{x}}$ as the *micro-diffusivity* constant for the bond $(\hat{\mathbf{x}}, \mathbf{x})$, i.e., the proportionality constant of the kernel. In scenarios involving N distinct species, the concentrations at $\mathbf{x}$ and time t are denoted by $c_k(\mathbf{x},t)$ for $k = 1, 2, \ldots, N$, where each species partakes in chemical reactions either as a reactant or product. The cumulative reaction term for the kth species at $\mathbf{x}$ is given by $R_k(\mathbf{x},t)$. Thus, the nonlocal Nernst-Planck system for the kth species, integrating diffusion, electromigration, and chemical reactions, is formulated as

$$\begin{aligned} \frac{\partial c_k(\mathbf{x},t)}{\partial t} = & \int_{\mathcal{H}_\mathbf{x}} \kappa_k(\hat{\mathbf{x}},\mathbf{x},t) \left(\frac{c_k(\hat{\mathbf{x}},t) - c_k(\mathbf{x},t)}{\|\hat{\mathbf{x}} - \mathbf{x}\|^2} + \frac{z_k F}{RT} \frac{\phi(\hat{\mathbf{x}}) - \phi(\mathbf{x})}{\|\hat{\mathbf{x}} - \mathbf{x}\|^2} \big(c_k(\hat{\mathbf{x}},t) + c_k(\mathbf{x},t) \big) \right) \mathrm{d}V_{\hat{\mathbf{x}}} \\ & + R_k(\mathbf{x},t), \end{aligned} \quad (12)$$

where the micro-diffusivity $\kappa(\hat{\mathbf{x}},\mathbf{x},t)$ can generally vary over time and space. To complete the N-component Nernst-Planck system with the electrostatic potential ϕ as an additional unknown, we adopt the Poisson-Boltzmann equation, often referred to as Gauss' law, as

$$-\nabla \cdot \sigma(\mathbf{x}) \nabla \phi(\mathbf{x}) = F \sum_{k=1}^{N} z_k c_k(\mathbf{x},t), \quad (13)$$

where $\sigma(\mathbf{x})$ denotes the electrical conductivity at $\mathbf{x}$. This model captures the electric field generated by the spatial distribution of ionic species. Assuming a uniform electric conductivity throughout the medium, and inspired by the nonlocal adaptation of Eq. 13 as previously demonstrated in works such as [39, 73], we can complete the N nonlocal Nernst-Planck equations from Eq. 12 using the nonlocal Poisson equation given by

$$-\int_{\mathcal{H}_\mathbf{x}} \epsilon \frac{\phi(\hat{\mathbf{x}}) - \phi(\mathbf{x})}{\|\hat{\mathbf{x}} - \mathbf{x}\|^2} \mathrm{d}V_{\hat{\mathbf{x}}} = F \sum_{k=1}^{N} z_k c_k(\mathbf{x},t), \quad (14)$$

where ϵ represents the *micro-conductivity* within the medium.

Remark 1 While deriving the nonlocal Nernst-Planck-Poisson system, we have omitted the contribution to the total flux due to any external advective flow, characterized by the velocity v. Should the system experience significant external flow fields, the nonlocal Nernst-Planck equation could be augmented by incorporating an advective integral term on its right-hand side. Following the methodology in [65, 71], this addition would be represented as

$$\begin{aligned} \frac{\partial c_k(\mathbf{x},t)}{\partial t} = \int_{\mathcal{H}_\mathbf{x}} \Big(& \kappa_k(\hat{\mathbf{x}},\mathbf{x},t) \frac{c_k(\hat{\mathbf{x}},t) - c_k(\mathbf{x},t)}{\|\hat{\mathbf{x}} - \mathbf{x}\|^2} - \nu_k(\hat{\mathbf{x}},\mathbf{x},t) \frac{c_k(\hat{\mathbf{x}},t) - c_k(\mathbf{x},t)}{\|\hat{\mathbf{x}} - \mathbf{x}\|} + \\ & \kappa_k(\hat{\mathbf{x}},\mathbf{x},t) \frac{z_k F}{RT} \frac{\phi(\hat{\mathbf{x}}) - \phi(\mathbf{x})}{\|\hat{\mathbf{x}} - \mathbf{x}\|^2} \big(c_k(\hat{\mathbf{x}},t) + c_k(\mathbf{x},t) \big) \Big) \mathrm{d}V_{\hat{\mathbf{x}}} + R_k(\mathbf{x},t), \end{aligned} \quad (15)$$

where $\nu_k(\hat{\mathbf{x}},\mathbf{x},t)$ signifies the *micro-velocity* for the bond $(\hat{\mathbf{x}}, \mathbf{x})$ relating to the kth ionic species. This micro-velocity, similar to micro-diffusivity, may vary with time and space. Equation 15 forms the comprehensive nonlocal diffusion-advection-electromigration-reaction model, which can be further complemented by the nonlocal Poisson equation detailed in

Eq. 14. For the purposes of this study, and in both numerical and experimental examples, the effects of the advective term are assumed negligible and thus not further considered.

3 Convergence in the Nonlocal to Local Limit

In this section, our discussion pivots towards a broader class of nonlocal Nernst-Planck-Poisson systems in 3D, with an emphasis on demonstrating their convergence to their local equivalents as the PD horizon $\delta \to 0$ becomes infinitesimally small. Define $\boldsymbol{\xi} := \hat{\mathbf{x}} - \mathbf{x}$ as the bond vector connecting points $\hat{\mathbf{x}}$ and $\mathbf{x}$, and introduce $\omega(\|\boldsymbol{\xi}\|)$ as a non-negative, radially symmetric *influence function*. This function plays a crucial role in PD constitutive modeling by weighting the influence of bonds based on their length [14, 58]. The generalized version of the nonlocal Nernst-Planck equation for the kth species, incorporating the weighted kernel functions, is given by

$$\frac{\partial c_k(\mathbf{x},t)}{\partial t} = \int_{\mathcal{H}_\mathbf{x}} \left[K_1 \omega(\|\boldsymbol{\xi}\|) D_k \frac{c_k(\hat{\mathbf{x}},t) - c_k(\mathbf{x},t)}{\|\boldsymbol{\xi}\|^{n+2s_1}} + K_2 \omega(\|\boldsymbol{\xi}\|) D_k \frac{z_k F}{RT} \frac{\phi(\hat{\mathbf{x}}) - \phi(\mathbf{x})}{\|\boldsymbol{\xi}\|^{n+2s_2}} \left(c_k(\hat{\mathbf{x}},t) + c_k(\mathbf{x},t) \right) \right] \mathrm{d}V_{\hat{\mathbf{x}}} + R_k(\mathbf{x},t), \tag{16}$$

where K_1 and K_2 are proportionality constants to be determined, n represents the spatial dimension, and s_1 and s_2 are the shape factors of the kernels, designed to resemble the formulation fractional diffusion equations. For a uniform influence function $\omega(\|\boldsymbol{\xi}\|) \equiv 1$, selecting $s_1 = s_2 = -1/2$, and setting $K_1 = K_2 = 1/V_{\mathcal{H}_\mathbf{x}}$, Eq. 16 aligns with the specific case presented in Eq. 12. This indicates that the latter represents a special case within the broader framework of Eq. 16. The nonlocal Poisson equation is similarly extended to encompass various kernel functions as

$$-\int_{\mathcal{H}_\mathbf{x}} K_3 \omega(\|\boldsymbol{\xi}\|) \sigma \frac{\phi(\hat{\mathbf{x}}) - \phi(\mathbf{x})}{\|\boldsymbol{\xi}\|^{n+2s_3}} \mathrm{d}V_{\hat{\mathbf{x}}} = F \sum_{i=1}^{N} z_k c_k(\mathbf{x},t), \tag{17}$$

where K_3 acts as the proportionality constant and s_3 is the shape factor for this equation. In the following, we aim to illustrate that, as nonlocal interactions diminish with δ approaching zero, the system in Eqs. 16 and 17 converges to the classical (local) Nernst-Planck-Poisson system of equations. This process involves utilizing Taylor series expansions for the nonlocal fluxes and determining the proportionality constants such that the leading-terms align with the classical counterparts, a methodology detailed in references such as [11, 57]. It should be noted that other approaches in the literature have already proposed recasting the local differential operator using nonlocal operators based on the peridynamic differential operator [40, 45, 60]. Our goal here is to demonstrate that the proposed system of equations is consistent and convergent to the local counterpart.

We begin by defining a spherical subregion $\mathcal{B}^{0,\delta}$ within a bounded body $\mathcal{B}$ as

$$\mathcal{B}^{0,\delta} := \{\mathbf{x} \in \mathcal{B} : \mathcal{H}(\mathbf{x},\delta) \subset \mathcal{B}\}. \tag{18}$$

For $\mathbf{x} \in \mathcal{B}^{0,\delta}$, consider a smoothly varying concentration field $c_k(\mathbf{x},t)$. For distances satisfying $\|\boldsymbol{\xi}\| \le \delta$, the concentration field can be expanded in form of a Taylor series as

$$c_k(\hat{\mathbf{x}},t) = c_k(\mathbf{x},t) + (\boldsymbol{\xi}\cdot\nabla)c_k(\mathbf{x},t) + \frac{1}{2}(\boldsymbol{\xi}\cdot\nabla)(\boldsymbol{\xi}\cdot\nabla)c_k(\mathbf{x},t) + \mathcal{O}\left(\|\boldsymbol{\xi}\|^3\right). \tag{19}$$

Inserting this expansion into the first term of the integrand from Eq. 16 and assuming the Einstein summation convention for repeated indices yields

$$\int_{\mathcal{H}_{\mathbf{x}}} K_1\omega(\|\boldsymbol{\xi}\|)D_k\frac{c_k(\hat{\mathbf{x}},t)-c_k(\mathbf{x},t)}{\|\boldsymbol{\xi}\|^{n+2s_1}}\mathrm{d}V_{\hat{\mathbf{x}}}=\left[\int_{\mathcal{H}} K_1\omega(\|\boldsymbol{\xi}\|)D_k\frac{\xi_i}{\|\boldsymbol{\xi}\|^{n+2s_1}}\mathrm{d}V_{\boldsymbol{\xi}}\right]\frac{\partial c_k(\mathbf{x},t)}{\partial x_i}$$
$$+\frac{1}{2}\left[\int_{\mathcal{H}} K_1\omega(\|\boldsymbol{\xi}\|)D_k\frac{\xi_i\xi_j}{\|\boldsymbol{\xi}\|^{n+2s_1}}\mathrm{d}V_{\boldsymbol{\xi}}\right]\frac{\partial^2 c_k(\mathbf{x},t)}{\partial x_i\partial x_j}+\mathcal{O}\left(\delta^2\right), \tag{20}$$

where a change in integration variables is employed and $\mathcal{H}$ denotes the spherical neighborhood with radius δ around the origin. The symmetry of the integration process causes all antisymmetric terms in Eq. 20 to vanish. This leaves the second-order partial derivatives as the primary contributors to the expansion, with the fourth-order partial derivatives following as the next significant terms affecting the truncation error. Assuming the 3D case, the bond vector $\boldsymbol{\xi}$ may be represented in spherical coordinates as $\boldsymbol{\xi}=\left(\xi_x,\xi_y,\xi_z\right)=r(\cos\theta\sin\varphi,\sin\theta\sin\varphi,\cos\varphi)$. Consequently, the coefficients of the second-order partial derivatives can be concisely written in matrix form as

$$\mathbf{M}=\frac{1}{2}\int_0^{\pi}\int_0^{2\pi}\int_0^{\delta}K_1\omega(r)\begin{bmatrix}\cos^2\theta\sin^2\varphi & \sin\theta\cos\theta\sin^2\varphi & \cos\theta\sin\varphi\cos\varphi\\ \sin\theta\cos\theta\sin^2\varphi & \sin^2\theta\sin^2\varphi & \sin\theta\sin\varphi\cos\varphi\\ \cos\theta\sin\varphi\cos\varphi & \sin\theta\sin\varphi\cos\varphi & \cos^2\varphi\end{bmatrix}\cdot$$
$$\frac{D_k}{r^{n+2s_1}}r^4\sin\varphi\,\mathrm{d}r\,\mathrm{d}\theta\,\mathrm{d}\varphi. \tag{21}$$

Due to the integration ranges, all non-diagonal entries of $\mathbf{M}$ vanish, leading to equal diagonal values. Thus, by choosing the proportionality constant as

$$K_1=2\left(\int_0^{\pi}\int_0^{2\pi}\int_0^{\delta}\omega(r)\frac{r^4}{r^{n+2s_1}}\cos^2\varphi\sin\varphi\,\mathrm{d}r\,\mathrm{d}\theta\,\mathrm{d}\varphi\right)^{-1}, \tag{22}$$

the matrix $\mathbf{M}$ with its entries M_{ij} is simplified to

$$M_{ij}=D_k\delta_{ij}, \tag{23}$$

where δ_{ij} represents the Kronecker delta. As $\delta\to 0$, we recover the Laplace operator

$$\lim_{\delta\to 0}M_{ij}\frac{\partial^2 c_k(\mathbf{x},t)}{\partial x_i\partial x_j}+\mathcal{O}(\delta^2)=D_k\frac{\partial^2 c_k(\mathbf{x},t)}{\partial x_j\partial x_j}, \tag{24}$$

thus demonstrating the model's convergence to the local Fickian diffusion term for the first integrand in Eq. 16. With a constant and unitary influence function $\omega(\|\boldsymbol{\xi}\|)$ and setting $n=3$ for the 3D scenario, an analytical expression for K_1 is derived as

$$K_1=\frac{3(1-s_1)}{\pi\delta^{2-2s_1}},\quad s_1<1. \tag{25}$$

In the subsequent step, we analyze the limit convergence behavior for the second integrand in Eq. 16. Utilizing the Taylor series expansion in Eq. 19 for both the concentration variable $c_k(\mathbf{x},t)$ and the electrostatic potential $\phi(\mathbf{x})$ at a point $\mathbf{x}\in\mathcal{B}^{0,\delta}$, and inserting these into the second integrand of Eq. 16, we obtain

$$\int_{\mathcal{H}_{\mathbf{x}}} K_2\omega(\|\boldsymbol{\xi}\|)D_k\frac{z_kF}{RT}\frac{\phi(\hat{\mathbf{x}})-\phi(\mathbf{x})}{\|\boldsymbol{\xi}\|^{n+2s_2}}\left(c_k(\hat{\mathbf{x}},t)+c_k(\mathbf{x},t)\right)\mathrm{d}V_{\hat{\mathbf{x}}}$$

$$
= \int_{\mathcal{H}_{\mathbf{x}}} K_2 \omega(\|\boldsymbol{\xi}\|) D_k \frac{z_k F}{RT} \frac{1}{\|\boldsymbol{\xi}\|^{n+2s_2}} \Big[2c_k(\mathbf{x},t) + (\boldsymbol{\xi}\cdot\nabla)c_k(\mathbf{x},t) + \frac{1}{2}(\boldsymbol{\xi}\cdot\nabla)(\boldsymbol{\xi}\cdot\nabla)c_k(\mathbf{x},t) + \dots \Big] \cdot \\
\Big((\boldsymbol{\xi}\cdot\nabla)\phi(\mathbf{x}) + \frac{1}{2}(\boldsymbol{\xi}\cdot\nabla)(\boldsymbol{\xi}\cdot\nabla)\phi(\mathbf{x}) + \dots \Big) \mathrm{d}V_{\hat{\mathbf{x}}}, \tag{26}
$$

Expanding the terms and considering the symmetry of the integration domain allows for the elimination of antisymmetric integrands within Eq. 26, the latter equation can be written as

$$
\int_{\mathcal{H}_{\mathbf{x}}} K_2 \omega(\|\boldsymbol{\xi}\|) D_k \frac{z_k F}{RT} \frac{\phi(\hat{\mathbf{x}}) - \phi(\mathbf{x})}{\|\boldsymbol{\xi}\|^{n+2s_2}} \left(c_k(\hat{\mathbf{x}},t) + c_k(\mathbf{x},t) \right) \mathrm{d}V_{\hat{\mathbf{x}}} \\
= \int_{\mathcal{H}} K_2 \omega(\|\boldsymbol{\xi}\|) D_k \frac{z_k F}{RT} \frac{\xi_i \xi_j}{\|\boldsymbol{\xi}\|^{n+2s_2}} \mathrm{d}V_{\boldsymbol{\xi}} \left(c_k(\mathbf{x},t) \frac{\partial^2 \phi(\mathbf{x})}{\partial x_i \partial x_j} + \frac{\partial c_k(\mathbf{x},t)}{\partial x_i} \frac{\partial \phi(\mathbf{x})}{\partial x_j} \right) + \mathcal{O}(\delta^2), \tag{27}
$$

adhering to the Einstein summation convention. Given the 3D case, we can once again articulate the coefficients related to the partial derivatives on the right-hand side in a matrix format, paralleling the approach taken with Eq. 21, ensuring that, due to symmetric integration ranges, non-diagonal terms are nullified and diagonal entries are equated. Hence, selecting an appropriate proportionality constant K_2 as

$$
K_2 = \left(\int_0^{\pi} \int_0^{2\pi} \int_0^{\delta} \omega(r) \frac{r^4}{r^{n+2s_2}} \cos^2\varphi \sin\varphi \, \mathrm{d}r \, \mathrm{d}\theta \, \mathrm{d}\varphi \right)^{-1}, \tag{28}
$$

aligns the second integrand in Eq. 16 with the electromigration-related fluxes within the classical Nernst-Planck model as $\delta \to 0$ approaches zero:

$$
\lim_{\delta\to 0} \left[\int_{\mathcal{H}} K_2 \omega(\|\boldsymbol{\xi}\|) D_k \frac{z_k F}{RT} \frac{\xi_i \xi_j}{\|\boldsymbol{\xi}\|^{n+2s_2}} \mathrm{d}V_{\boldsymbol{\xi}} \right] \left(c_k(\mathbf{x},t) \frac{\partial^2 \phi(\mathbf{x})}{\partial x_i \partial x_j} + \frac{\partial c_k(\mathbf{x},t)}{\partial x_i} \frac{\partial \phi(\mathbf{x})}{\partial x_j} \right) + \mathcal{O}(\delta^2) \\
= D_k \frac{z_k F}{RT} \left(c_k(\mathbf{x},t) \frac{\partial^2 \phi(\mathbf{x})}{\partial x_j \partial x_j} + \frac{\partial c_k(\mathbf{x},t)}{\partial x_j} \frac{\partial \phi(\mathbf{x})}{\partial x_j} \right). \tag{29}
$$

Note that, when s_1 matches s_2, the proportionality constants K_1 and K_2 coincide. Assuming a uniform influence function, we may derive K_2 for the 3D case as

$$
K_2 = \frac{3(1-s_2)}{\pi \delta^{2-2s_2}}, \quad s_2 < 1. \tag{30}
$$

Employing the methodology utilized for the nonlocal Nernst-Planck equation, an analogous convergence analysis can be conducted for the nonlocal Poisson equation in Eq. 14, thus demonstrating the model's ability to converge to its classical equivalents in the nonlocal to local limit. Nevertheless, to maintain focus and conciseness, we do not include this derivation within the current discussion and refer to the respective literature [26, 61]. The same procedure is applicable for 1D and 2D settings, however, given our emphasis on the general 3D case, theoretical explorations into 1D and 2D configurations are omitted here as well.

4 Constitutive Peridynamic Corrosion Modeling

The NNPP system, represented in Eqs. 16 and 17, enables us to simulate electrochemical corrosion and anodic dissolution of diverse metallic materials in aqueous environments, thus constituting a generalization of the PD diffusion-based bi-material corrosion model. For the NNPP equations to accurately reflect the complex dynamics of corrosion, they have to incorporate constitutive assumptions that precisely capture the interface kinetics specific to each corrosion system. The standard PD bi-material corrosion model based on a homogenization approach uses a solid-liquid interface description, which effectively describes anodic dissolution, surface conversion, and layer deposition efficiently [27, 51]. The computational domain is thus separated into two phases: the metallic phase, indicated by a phase variable $\varphi = 1$, and the surrounding liquid electrolyte, with $\varphi = 0$. The separation allows for description of the transitional zone at the corrosion interface between solid and liquid phases, referred to as the *diffusive corrosion layer* (DCL), where chemical composition and mechanical properties change. Illustrated in Fig. 2, the DCL is defined by a 2δ boundary around the phase separation line, highlighting the area where ionic transport of metal ions into the electrolyte occurs. Within the PD neighborhood with a horizon of δ, material points are establish nonlocal bond interactions across different phases, leading to distinctions between solid-solid, liquid-liquid, and interface bonds, as visualized in Fig. 2. Moreover, the interfacial effects associated with the formation of the electrical double layer are implicitly modeled through the electrostatic potential distribution and ionic concentration gradients across the interface in the DCL.

The domain separation in the NNPP system is adapted to resemble the approach taken in PD bi-material corrosion models, as visualized in Fig. 2. Within the domain, bonds are conceptualized as conduits between *concentration buckets*, endowed with specific constitutive properties that govern species transport. These properties cover aspects related to the dynamics of solid metal surface wetting and the impact of microstructural defects, including microcracks, pores, and precipitates, on material degradation [13, 70]. In deploying the nonlocal Nernst-Planck system for PD corrosion modeling, we adopt a constitutive relation at the bond level, particularly through the specification of the Fickian diffusion coefficient. This is exemplified by defining the time-dependent diffusion coefficient $D_{k,ij}(t)$ for the kth species associated with a bond vector $\boldsymbol{\xi} := \mathbf{x}_j - \mathbf{x}_i$, as

$$D_{k,ij}(t) = \begin{cases} D_{k,l}, & \varphi(\mathbf{x}_j, t) = 0 \wedge \varphi(\mathbf{x}_i, t) = 0 \\ D_{k,i}(t), & \varphi(\mathbf{x}_j, t) = 1 \oplus \varphi(\mathbf{x}_i, t) = 1 \\ D_{k,s}, & \varphi(\mathbf{x}_j, t) = 1 \wedge \varphi(\mathbf{x}_i, t) = 1 \end{cases}, \tag{31}$$

where $D_{k,l}$ and $D_{k,s}$ denote the diffusion coefficients for liquid-liquid and solid-solid bonds, respectively, for the kth species, and are considered constant throughout the corrosion system

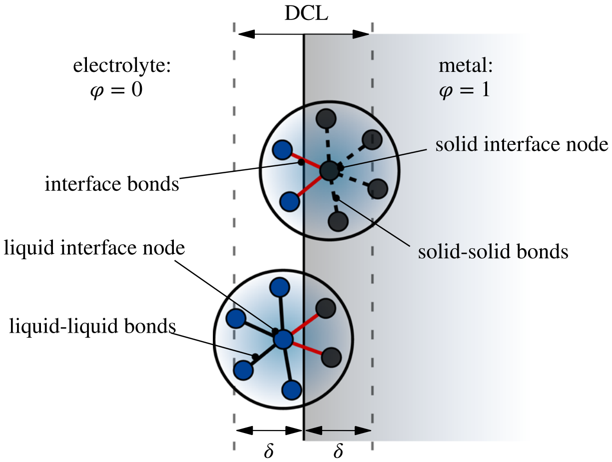

Fig. 2 A schematic representation of the diffusive corrosion layer and spherical neighborhoods with different bond types across the corrosion interface

and in the numerical examples presented below. The effective interface diffusivity $D_{k,i}(t)$ reflects constitutive assumptions tailored to the specific corrosion system under study. This approach to defining the diffusion coefficient, as set out in Eq. 31, also applies to the electrical conductivity σ within the nonlocal Poisson equation. This approach thus provides the constitutive interface to accurately represent metallic ion dissolution and the distribution of electrostatic potential in the electrolyte. In Sections 6 and 7, we examine two distinct corrosion systems, developing constitutive relations that effectively encapsulate the involved processes. Although these models are adaptable to a wide range of corrosion scenarios by incorporating various assumptions, it is important to acknowledge that the diffusion coefficients are modulated by the phase change parameter φ, thereby necessitating an appropriate phase change mechanism within the model. In keeping with standard PD corrosion model conventions, a phase transition from metal to liquid occurs if the metal ion concentration dips below the saturation concentration in the liquid, as exemplified by [27] as

$$\varphi(\mathbf{x}, t) = \begin{cases} 1, & c_1(\mathbf{x}, t) \geq c_{\text{sat}} \\ 0, & c_1(\mathbf{x}, t) < c_{\text{sat}} \end{cases}, \tag{32}$$

where c_{sat} is the saturation concentration of metal ions in the liquid electrolyte, and without loss of generality $c_1(\mathbf{x}, t)$ represents the concentration of metal ions at point $\mathbf{x}$ and time t. This mechanism is employed throughout the numerical examples of our study.

5 Numerical Implementation

In this section, we present the discrete formulation of the governing equations from Eqs. 16 to 17 and introduce an efficient numerical scheme for handling 3D problems. We apply a time-implicit discretization to the nonlocal Nernst-Planck equation presented in Eq. 16 for the field variable $c_k(\mathbf{x}, t)$, while the electrostatic potential $\phi(\mathbf{x})$ and the nonlinear interactions with other species through reaction terms are treated explicitly. This semi-implicit approach reduces the number of unknowns needed for updating the kth species, ensuring both accuracy and numerical stability. The integral term is approximated using a modified one-point Gaussian summation rule, referred to as the *standard meshfree discretization* in PD modeling [41], as illustrated schematically in Fig. 3. Consequently, the governing equation in its discretized residual form is expressed as

$$\begin{aligned} F_{c,i}(c^{n+1}_{k,i}) :=& \frac{c^{n+1}_{k,i} - c^{n}_{k,i}}{\Delta t} - \sum_{j \in \mathcal{F}_i} \Bigg[K_1 \omega(\|\mathbf{x}_j - \mathbf{x}_i\|) D^n_{k,ji} \frac{c^{n+1}_{k,j} - c^{n+1}_{k,i}}{\|\mathbf{x}_j - \mathbf{x}_i\|^{n+2s_1}} \\ &+ K_2 \omega(\|\mathbf{x}_j - \mathbf{x}_i\|) D^n_{k,ji} \frac{z_k F}{RT} \frac{\phi_j - \phi_i}{\|\mathbf{x}_j - \mathbf{x}_i\|^{n+2s_2}} \left(c^{n+1}_{k,j} + c^{n+1}_{k,i} \right) \Bigg] \Delta \mathrm{V}_j - R^{n+1}_{k,i} = 0, \end{aligned}$$

indicating $c^{n+1}_{k,i} := c_k(\mathbf{x}_i, t^{n+1})$ where the time step is marked by the upper index and spatial location by the lower indices for the kth species, and the comma index notation is purely spatial, not indicating differentiation. Here, $D^n_{k,ji}$ signifies the Fickian diffusion coefficient of the kth species for the bond $\boldsymbol{\xi} := \mathbf{x}_j - \mathbf{x}_i$ at time t^n, which can vary over time and space, and ΔV_j represents the cell volume around the neighbor point $\mathbf{x}_j$ within the neighborhood $\mathcal{F}_i$ of point $\mathbf{x}_i$. The term $R^{n+1}_{k,i}$ includes the reaction contributions of the kth species at point $\mathbf{x}_i$, treating explicit dependencies on the kth species concentration implicitly in time, while other species are treated explicitly. The Newton-Raphson method is employed for solving the algebraic equation in Eq. 33, necessitating a preliminary linearization of the equation as

$$\mathbf{F}_c(\mathbf{c}^{n+1}_k) \approx \mathbf{F}_c(\mathbf{c}^n_k) + \mathbf{K}_c(\mathbf{c}^n_k) \Delta \mathbf{c} = \mathbf{0}, \tag{33}$$

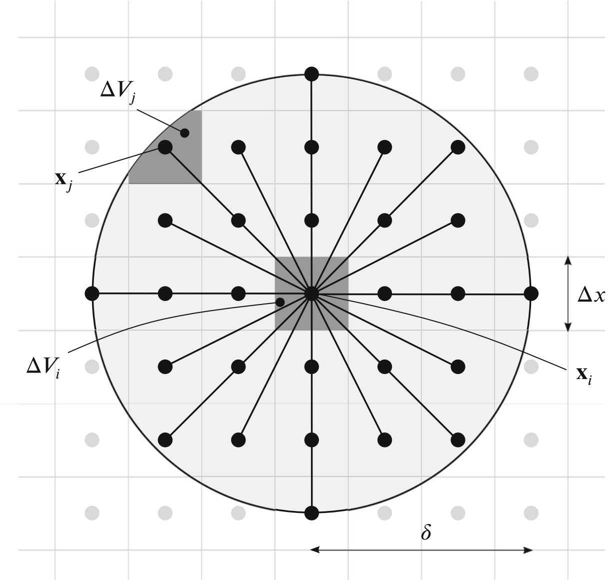

Fig. 3 A schematic depiction of the neighborhood surrounding node $\mathbf{x}_i$ on a regular 2D grid, characterized by grid spacing Δx and the associated cell volume ΔV_i. Reproduced from [27]

with the vector $\mathbf{c}_k^{n+1}$ encompassing nodal concentrations of species k across the computational domain as

$$\mathbf{c}_k^{n+1} := \begin{pmatrix} c_{k,1}^{n+1} \\ c_{k,2}^{n+1} \\ \vdots \\ c_{k,j}^{n+1} \\ \vdots \\ c_{k,N_p}^{n+1} \end{pmatrix}, \tag{34}$$

where N_p denotes the total number of nodal points in the computational domain. Similarly, $\mathbf{F}_c(\mathbf{c}_k^{n+1})$ refers to the global residual vector associated with the kth species across all nodal points within the computational domain for the time step at t^{n+1}. The Jacobian matrix in Eq. 33 is denoted as $\mathbf{K}_c(\mathbf{c}_k^n)$, and $\Delta\mathbf{c}$ is the incremental update. The entries of the Jacobian matrix are initialized at the start of each time step as

$$K_{c,ii} = \frac{\partial F_{c,i}(c_{k,i}^{n+1})}{\partial c_{k,i}^{n+1}} = \frac{1}{\Delta t} - \sum_{j\in\mathcal{F}_i}\Bigg[-K_1\omega(\|\mathbf{x}_j-\mathbf{x}_i\|)\frac{D_{k,ji}^n}{\|\mathbf{x}_j-\mathbf{x}_i\|^{n+2s_1}} + K_2\omega(\|\mathbf{x}_j-\mathbf{x}_i\|)D_{k,ji}^n\frac{z_kF}{RT}\frac{\phi_j-\phi_i}{\|\mathbf{x}_j-\mathbf{x}_i\|^{n+2s_2}}\Bigg]\Delta V_j - \frac{\partial R_{k,i}^{n+1}}{\partial c_{k,i}^{n+1}}, \tag{35}$$

$$K_{c,ij} = \frac{\partial F_{c,i}(c_{k,i}^{n+1})}{\partial c_{k,j}^{n+1}} = -\Bigg[-K_1\omega(\|\mathbf{x}_j-\mathbf{x}_i\|)\frac{D_{k,ji}^n}{\|\mathbf{x}_j-\mathbf{x}_i\|^{n+2s_1}}$$

$$+ K_2\omega(\|\mathbf{x}_j - \mathbf{x}_i\|) D^n_{k,ji} \frac{z_k F}{RT} \frac{\phi_j - \phi_i}{\|\mathbf{x}_j - \mathbf{x}_i\|^{n+2s_2}} \Bigg] \Delta V_j, \tag{36}$$

indicating $K_{c,ii}$ and $K_{c,ij}$ as the diagonal and off-diagonal entries of the Jacobian matrix, $\mathbf{K}_c$. For the initial step of the Newton-Raphson iteration, the first approximation of the concentration vector, $\mathbf{c}_k^{n+1,m=0}$, is set to the preceding time step's results

$$\mathbf{c}_k^{n+1,m=0} = \mathbf{c}_k^{n+1,0} = \mathbf{c}_k^n, \tag{37}$$

where we use the index m to denote iterations within the Newton-Raphson method. The concentration vector undergoes successive updates at each iteration by resolving the linear system given in Eq. 38 as

$$\begin{aligned} \Delta\mathbf{c} &= -\mathbf{K}_c^{-1}(\mathbf{c}_k^{n,0})\mathbf{F}_c(\mathbf{c}_k^{n+1,m}) \\ \mathbf{c}_k^{n+1,m+1} &= \mathbf{c}_k^{n+1,m} + \lambda\Delta\mathbf{c}, \end{aligned} \tag{38}$$

with the Jacobian matrix $\mathbf{K}_c$ being computed at the start of the iteration and subsequently assumed constant. The relaxation factor λ, set within the range $(0, 1]$, is chosen as $\lambda = 1$ for all numerical results presented in this work. Following the approach used for the nonlocal Nernst-Planck equation, the nonlocal Poisson equation presented in Eq. 17 is discretized in space using the standard meshfree discretization technique of PD modeling. This yields the residual formulation for at point $\mathbf{x}_i$ as

$$F_{\phi,i}(\phi_i) := -\sum_{j\in\mathcal{F}_i} \left[K_3\omega(\|\mathbf{x}_j - \mathbf{x}_i\|) \frac{\sigma^n_{ji}}{\|\mathbf{x}_j - \mathbf{x}_i\|^{n+2s_3}} \left(\phi_j - \phi_i\right) \right] \Delta V_j - F \sum_{k=1}^{N} z_k c^n_{k,i} = 0, \tag{39}$$

where σ^n_{ji} represents the electrical conductivity for the bond $\mathbf{x}_j - \mathbf{x}_i$ at the time step t^n, generally varying over space and time. Equation 39 outlines a linear system which has to be solved at each time step by

$$\boldsymbol{\phi} = \mathbf{K}_\phi^{-1}\mathbf{b}_\phi, \tag{40}$$

with $\boldsymbol{\phi}$ indicating the global vector of electrostatic potential at the nodes and $\mathbf{b}_\phi$ is the right-hand-side vector defined by

$$\mathbf{b}_\phi = F \begin{pmatrix} \sum_{k=1}^N z_k c^n_{k,1} \\ \sum_{k=1}^N z_k c^n_{k,2} \\ \vdots \\ \sum_{k=1}^N z_k c^n_{k,j} \\ \vdots \\ \sum_{k=1}^N z_k c^n_{k,N_p} \end{pmatrix}, \tag{41}$$

and $\mathbf{K}_\phi^{-1}$ signifying the inverse of the conductance matrix. The element entries of the Jacobian matrix are given by

$$\begin{aligned} K_{\phi,ii} &= \sum_{j\in\mathcal{F}_i} \left[K_3\omega(\|\mathbf{x}_j - \mathbf{x}_i\|) \frac{\sigma^n_{ji}}{\mathbf{x}_j - \mathbf{x}_i\|^{n+2s_3}} \right] \Delta V_j \\ K_{\phi,ij} &= -K_3\omega(\|\mathbf{x}_j - \mathbf{x}_i\|) \frac{\sigma^n_{ji}}{\|\mathbf{x}_j - \mathbf{x}_i\|^{n+2s_3}} \Delta V_j. \end{aligned} \tag{42}$$

It should be noted that, the integration of boundary conditions, whether Dirichlet or Neumann, into Eqs. 38 and 40 necessitates adjustments to the system matrices $\mathbf{K}_c$ and $\mathbf{K}_\phi$ and the right-hand-sides $\mathbf{F}_c$ and $\mathbf{b}_\phi$. A detailed methodology for incorporating boundary conditions can be found in [27]. The accurate embedding of Neumann-type boundary conditions in nonlocal models remains the subject of ongoing debate, with further information available in the respective literature [52, 61, 66, 72].

6 1D Pencil Electrode Corrosion

In this section, we apply the NNPP system, as formulated in Eqs. 16 and 17, to model the corrosion process of a 1D pencil electrode. This experimental setup has been previously explored in [18, 19] and utilized to benchmark corrosion models, particularly those based on phase-field methods [7]. Accordingly, we adopt this scenario as idealized corrosion system to assess the NNPP system's efficacy towards general corrosion modeling. The experimental data and model parameters largely align with the phase field study in [7] and are detailed in Table 2. The experiment simulates 1D pencil electrode corrosion at 20°with a metal potential of 844 mV in a 1 M NaCl electrolyte solution. Following the classical Butler-Volmer (BV) equation for anodic dissolution, presented as

$$i_a = i_0 \left[\exp\left(\frac{\alpha_a z_1 F \eta}{RT} \right) - \exp\left(-\frac{\alpha_c z_1 F \eta}{RT} \right) \right], \tag{43}$$

where i_a denotes the anodic current density, i_0 is the exchange current density, α_a and α_c are the anodic and cathodic charge transfer coefficients, respectively, η represents the overpotential, and z_1 is the charge number of the metal ion involved. We adopt the BV kinetics as an idealized approximation to validate the performance of the proposed NNPP equations. It is important to recognize that the actual corrosion kinetics of a given system may require a much more complex relationship than that described by the BV equation. According to [13], the anodic current described by Eq. 43 is linearly dependent on the effective ionic diffusivity, thus providing a linear correlation between the diffusion coefficient and the anodic dissolution current density. Substituting this linear relationship yields an Arrhenius-type expression for the diffusion coefficient as

$$D(\eta) = D_0 \left[\exp\left(\frac{\alpha_a z_1 F \eta}{RT} \right) - \exp\left(-\frac{\alpha_c z_1 F \eta}{RT} \right) \right], \tag{44}$$

with D_0 being the diffusion coefficient at zero overpotential. Following the assumption in [7], two cathodic reactions are proposed within the liquid electrolyte as

$$2\mathrm{H}^+ + 2\mathrm{e}^- \rightarrow \mathrm{H}_2, \tag{45}$$

$$2\mathrm{H}_2\mathrm{O} + 2\mathrm{e}^- \rightarrow \mathrm{H}_2 + 2\mathrm{OH}^-, \tag{46}$$

where Eq. 45 corresponds to hydrogen discharge near the corrosion surface, and Eq. 46 to the water reduction process. The reaction for hydrogen discharge is considered at material points near the corrosion interface, identified within a δ distance from the interface in the electrolyte phase ($\varphi = 0$) that establish nonlocal interactions with points within the metallic solid phase ($\varphi = 1$). The δ parameter thus represents a length scale determining the corrosion and precipitation layer thickness and can be correlated with experimental findings [16, 22, 27]. In our example, we further account for two reactions occurring within the electrolyte given by

$$\mathrm{Me}^{z_1} + \mathrm{H_2O} \rightleftharpoons \mathrm{MeOH}^{z_2} + \mathrm{H}^+, \tag{47}$$

$$\mathrm{H_2O} \rightleftharpoons \mathrm{OH}^- + \mathrm{H}^+, \tag{48}$$

which represent the oxidation of the metal leading to corrosion product formation and the self-dissociation of water, respectively. The comprehensive electrochemical corrosion model incorporates seven field variables, defined as

$$\begin{aligned} c_1 &= [\mathrm{Me}^{z_1}], \\ c_2 &= [\mathrm{MeOH}^{z_2}], \\ c_3 &= [\mathrm{Cl}^{z_3}], \\ c_4 &= [\mathrm{Na}^{z_4}], \\ c_5 &= [\mathrm{H}^{z_5}], \\ c_6 &= [\mathrm{OH}^{z_6}], \end{aligned} \tag{49}$$

where $c_1, c_2, \ldots, c_6$ represent the molar concentrations of species in the domain, with $z_1, z_2, \ldots, z_6$ being their respective charge numbers, and ϕ, the electrostatic potential, as the seventh field variable. Given the reactions outlined in Eqs. 45 and 46, we define the reaction terms $R_{1,i}^{n+1}$ for $c_{1,i}^{n+1}$ and $R_{2,i}^{n+1}$ for $c_{2,i}^{n+1}$ at the spatial point $\mathbf{x}_i$ and for time t^{n+1}, in line with the terms adapted from from [7], which are expressed as

$$R_{1,i}^{n+1} = \begin{cases} -k_{1f} c_{1,i}^{n+1} + k_{1b} c_{2,i}^{n} c_{5,i}^{n}, & \varphi(\mathbf{x}_i, t^n) = 0 \vee \exists \mathbf{x} \in \mathcal{F}_i : \varphi(\mathbf{x}_i, t^n) \neq \varphi(\mathbf{x}, t^n) \\ 0, & \varphi(\mathbf{x}_i, t^n) = 1 \wedge \forall \mathbf{x} \in \mathcal{F}_i : \varphi(\mathbf{x}, t^n) = 1 \end{cases}, \tag{50}$$

$$R_{2,i}^{n+1} = \begin{cases} k_{1f} c_{1,i}^{n} - k_{1b} c_{2,i}^{n+1} c_{5,i}^{n}, & \varphi(\mathbf{x}_i, t^n) = 0 \vee \exists \mathbf{x} \in \mathcal{F}_i : \varphi(\mathbf{x}_i, t^n) \neq \varphi(\mathbf{x}, t^n) \\ 0, & \varphi(\mathbf{x}_i, t^n) = 1 \wedge \forall \mathbf{x} \in \mathcal{F}_i : \varphi(\mathbf{x}, t^n) = 1 \end{cases}, \tag{51}$$

where k_{1f} and k_{1b} denote the forward and backward rates for the reaction provided in Eq. 47, related through the equilibrium constant $K_1 = k1f/k_{1b}$. These reaction terms are employed in the semi-implicit time discretization framework and are exclusively applied within the liquid electrolyte phase. As the chloride and sodium concentrations (c_3 and c_4) are non-reactive, their respective reaction rates remain zero throughout the domain. The reaction terms for c_5 and c_6 are determined in accordance with [7], following the reactions detailed in Eqs. 45 to 46 and 47 to 48, and are expressed as

$$\begin{gathered} R_{5,i}^{n+1} = \begin{cases} A_i^{n+1}, & \varphi(\mathbf{x}_i, t^n) = 0 \wedge \forall \mathbf{x} \in \mathcal{F}_i : \varphi(\mathbf{x}, t^n) = 0 \\ A_i^{n+1} + \dfrac{J_{50}}{z_5 F c_{\mathrm{solid}}} \exp\left(\dfrac{\alpha_{\mathrm{H}^+} F}{RT} \eta_i^n \right), & \exists \mathbf{x} \in \mathcal{F}_i : \varphi(\mathbf{x}_i, t^n) \neq \varphi(\mathbf{x}, t^n) \\ 0, & \varphi(\mathbf{x}_i, t^n) = 1 \wedge \forall \mathbf{x} \in \mathcal{F}_i : \varphi(\mathbf{x}, t^n) = 1 \end{cases}, \\ A_i^{n+1} = k_{1f} c_{1,i}^{n} - k_{1b} c_{2,i}^{n} c_{5,i}^{n+1} + k_{2f} - k_{2b} c_{5,i}^{n+1} c_{6,i}^{n} \end{gathered} \tag{52}$$

where k_{2f} and k_{2b} represent the forward and backward reaction rates of Eq. 48, and are related through the equilibrium constant $K_2 = k_{2f}/k_{2b}$, J_{50} is the proportionality factor at zero overpotential, c_{solid} denotes the initial metal solid concentration of the intact specimen, α_{H^+} represents the charge coefficient of the hydrogen ion, and η_i^n indicates the overpotential at point $\mathbf{x}_i$ and time instance t^n. Similarly, the reaction term for the hydroxide ion concentration c_6 is expressed as

$$
R_{6,i}^{n+1} = \begin{cases} B_i^{n+1}, & \varphi(\mathbf{x}_i, t^n) = 0 \wedge \forall \mathbf{x} \in \mathcal{F}_i : \varphi(\mathbf{x}, t^n) = 0 \\ B_i^{n+1} + \dfrac{J_{60}}{z_6 F c_{\text{solid}}} \exp\left(\dfrac{\alpha_{\text{OH}^-} F}{RT} \eta_i^n\right), & \exists \mathbf{x} \in \mathcal{F}_i : \varphi(\mathbf{x}_i, t^n) \neq \varphi(\mathbf{x}, t^n) \\ 0, & \varphi(\mathbf{x}_i, t^n) = 1 \wedge \forall \mathbf{x} \in \mathcal{F}_i : \varphi(\mathbf{x}, t^n) = 1 \end{cases},
$$
$$
B_i^{n+1} = k_{2f} - k_{2b} c_{5,i}^n c_{6,i}^{n+1}, \tag{53}
$$

where J_{60} is the proportionality factor at zero overpotential, and α_{OH^-} denotes the charge coefficient of the hydroxide ion. The electric overpotential is calculated as

$$
\eta_i^n = \phi_{\text{applied}} - \phi_0 - \phi_{c,i}^n - \phi_i, \tag{54}
$$

where ϕ_{applied} denotes the applied potential in the solid metal electrode, ϕ_0 stands for the reference potential in the metal, and $\phi_{c,i}^n$ indicates the concentration overpotential at point $\mathbf{x}_i$ and time instance t^n of the metallic solid phase expressed as

$$
\phi_{c,i}^n = \frac{RT}{z_1 F} \ln\left(\frac{c_{1,i}^n}{c_{\text{sat}}}\right), \tag{55}
$$

where c_{sat} represents the saturation concentration at equilibrium in the liquid electrolyte phase, and ϕ_i is the electrostatic potential at point $\mathbf{x}_i$, obtained through the nonlocal Poisson equation in Eq. 17 at time instance t^n.

6.1 Numerical Simulation Results for 1D Pencil Electrode

The numerical simulation covered 400 s on the computational domain in the interval [0, 200] µm, with a spatial discretization of $\Delta x = 0.25$ µm, resulting in 801 spatial nodes. The time step size was chosen to be $\Delta t = 0.5$ s. The PD horizon was chosen as $\delta = 1.25$ µm which is indicative of the measure of the corrosion and precipitation layer thickness. Initially, the subdomain [0, 175] µm is assigned to be intact metal material, denoted by phase $\varphi = 1$, while the remaining portion represents liquid electrolyte consisting of dilute salt water with a 1 M NaCl solution, thus $\varphi = 0$. Detailed initial and boundary conditions are provided in Appendix A, Table 1, and the model parameters are listed in Table 2. The constitutive relation for the diffusivity of interface bonds is given by a diffusion coefficient described by an Arrhenius-type equation derived from the BV relation, as outlined in Eq. 44. Figure 4 presents a comparison between the simulation results for the corroded length and experimental findings [7, 19]. Throughout the simulation duration, our results closely align with experimental observations, demonstrating a linear correlation between the corroded length of the 1D pencil electrode and the square root of simulation time, expressed as $L \propto \sqrt{t}$, where L denotes the corroded length.

In Fig. 5, we depict the numerical simulation results illustrating the distribution of ionic species within the liquid electrolyte phase at $t = 200$ s. As experimental data regarding the concentration of ionic components are unavailable for this corrosion system, our numerical predictions serve as a qualitative analysis, drawing comparisons with other numerical corrosion models, particularly those based on the PF approach. Although the results are not experimentally validated, our results qualitatively agree with the findings reported in [7], suggesting the same concentration ranges. In particular, our simulation results reveal higher

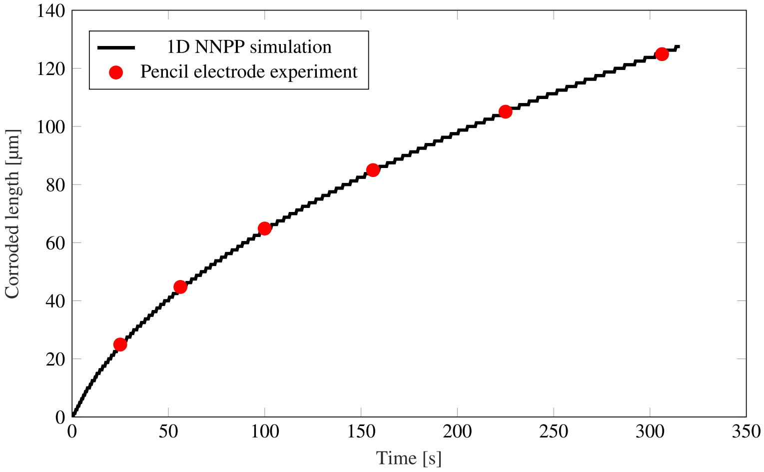

Fig. 4 Comparison of the corrosion length between the 1D NNPP model and the experimental pencil electrode data in 1 M NaCl solution at 20 °C as reported in [7, 19]

concentration of hydrogen ions near the corrosion interface, attributed to metal ion dissolution and hydrolysis and counteracted by the migration of chloride ions toward the interface, resulting in a reduction of pH value, in agreement with experimental observations and consistent with predictions from other numerical studies, i.e., comparable phase-field corrosion models.

7 3D Bone Implant Screw Degradation in Simulated Body Fluid

In this section, we employ a 3D NNPP system to model and simulate the *in vitro* degradation of a M2 × 4 mm headless bone implant screw made from a Mg-10Gd binary magnesium alloy, containing 10% gadolinium, under physiological conditions. Experimental details,

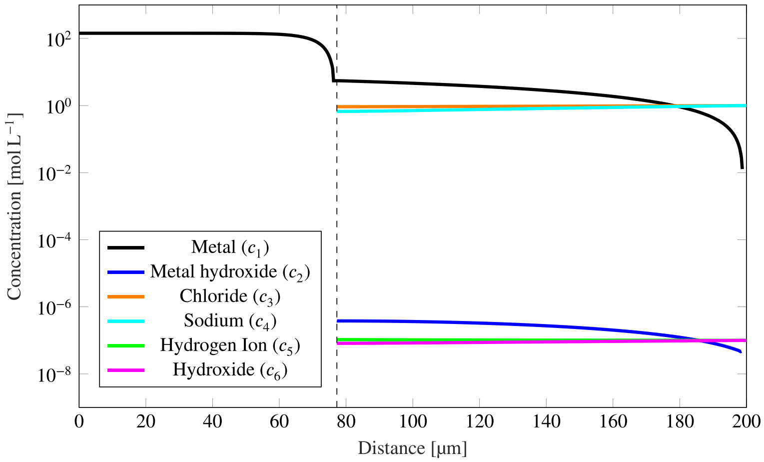

Fig. 5 Ionic species concentration at $\phi_{\text{applied}} = -300\,\text{mV}$ SHE and $t = 200\,\text{s}$

including a μCT analysis of microstructure and overall volume loss over an 8-week immersion period, are provided in [27, 38]. The bone implant samples are immersed in SBF, mimicking physiological conditions. Chemical composition and ionic concentrations of SBF are detailed in [69] and utilized for initial and boundary conditions in the numerical simulation, listed in Table 3 in Appendix B. The immersion process is quasi-static, with regular electrolyte refreshment to prevent ion depletion or salt saturation in the medium [38]. This setup mimics tissue hydrodynamics without convective flow, controlling salt and deposit formation during degradation based on the ions present. In our modeling of the electrochemical degradation of Mg-10Gd samples in SBF, we assume homogenized gadolinium inclusions and omit direct modeling of their effects. Following the model proposed in [69], the corrosion system is characterized by chemical and electrochemical reactions. Magnesium ion dissolution into the liquid electrolyte, accompanied by hydrogen gas formation, is described by

$$\mathrm{Mg(s)} \rightarrow \mathrm{Mg^{2+}(aq)} + 2\mathrm{e^-}, \tag{56}$$

$$2\mathrm{H^+(aq)} + 2\mathrm{e^-} \rightarrow \mathrm{H_2} \tag{57}$$

where (s) denotes a solid state and (aq) an aqueous phase. Unlike most corrosion models employed in the respective literature, our approach not only considers the formation of magnesium hydroxide but also encompasses several other precipitating components within the corrosive system, described by

$$\mathrm{Mg^{2+}(aq)} + 2\mathrm{OH^-(aq)} \rightarrow \mathrm{Mg(OH)_2(s)}, \tag{58}$$

$$\mathrm{Mg^{2+}(aq)} + \mathrm{HCO_3^-(aq)} \rightarrow \mathrm{Mg(CO)_3(s)} + \mathrm{H^+(aq)}, \tag{59}$$

$$\mathrm{Mg^{2+}(aq)} + \mathrm{HCO_3^-(aq)} + 3\mathrm{H_2O} \rightarrow \mathrm{Mg(HCO)_3OH} \cdot 2\mathrm{H_2O(s)} + \mathrm{H^+(aq)}, \tag{60}$$

$$3\mathrm{Mg^{2+}(aq)} + 2\mathrm{HPO_4^{2-}(aq)} + 8\mathrm{H_2O} \rightarrow \mathrm{Mg_3(PO_4)_2} \cdot 8\mathrm{H_2O(s)} + 2\mathrm{H^+(aq)}, \tag{61}$$

$$\mathrm{Ca^{2+}(aq)} + 2\mathrm{OH^-(aq)} \rightarrow \mathrm{Ca(OH)_2(s)} \tag{62}$$

$$\mathrm{Ca^{2+}(aq)} + \mathrm{HCO_3^-(aq)} \rightarrow \mathrm{CaCO_3(s)} + \mathrm{H^+(aq)} \tag{63}$$

$$5\mathrm{Ca^{2+}(aq)} + 3\mathrm{HPO_4^{2-}(aq)} + \mathrm{H_2O} \rightarrow \mathrm{Ca_5OH(PO_4)_3(s)} + 4\mathrm{H^+(aq)}, \tag{64}$$

incorporating the precipitation of brucite (*cf.* Eq. 58), magnesite (*cf.* Eq. 59), nesquehonite (*cf.* Eq. 60), bobierrite (*cf.* Eq. 61), portlandite (*cf.* Eq. 62), calcite (*cf.* Eq. 63), and hydroxyapatite (*cf.* Eq. 64). The corresponding dissolution equilibrium constants, expressed as logarithmic pK values at 37 °C, are adopted and refined from [36, 69] and are listed in Table 4. Additionally, we also consider the dissociation of water, hydrogen carbonate, and hydrogen phosphate within the liquid electrolyte environment as

$$\mathrm{H_2O} \rightleftharpoons \mathrm{H^+} + \mathrm{OH^-} \tag{65}$$

$$\mathrm{HCO_3^-} \rightleftharpoons \mathrm{CO_3^{2-}} + \mathrm{H^+} \tag{66}$$

$$\mathrm{HPO_4^{2-}} \rightleftharpoons \mathrm{PO_4^{3-}} + \mathrm{H^+}. \tag{67}$$

It is important to note that the local chemical conditions, such as pH level and temperature T, dictate which compounds precipitate either on the implant's surface - forming what is known as the degradation layer - or within the bulk of the electrolyte. The precipitation layer acts as a as a partially protective film around the implant, with its thickness and composition significantly affecting the rate and extent of corrosion. However, to determine whether all chemical reactions from Eqs. 58 to 64 need to be computed, a numerical analysis in [69] was conducted. This analysis assessed the fractions of precipitates forming in SBF at $T = 37\,°\mathrm{C}$ depending on the pH value and was further corroborated with experimental results. It was concluded that portlandite does not manifest in corrosion experiments of bio-degradable materials and is, therefore, excluded from this study. In total, the system comprises 11 unknown field variables, represented by the 10 unknown concentration distributions as

$$\begin{aligned}
c_1 &= [\mathrm{Mg}^{z1}],\\
c_2 &= [\mathrm{H}^{z2}],\\
c_3 &= [\mathrm{OH}^{z3}],\\
c_4 &= [\mathrm{HCO}_3^{z4}],\\
c_5 &= [\mathrm{CO}_3^{z5}],\\
c_6 &= [\mathrm{HPO}_4^{z6}],\\
c_7 &= [\mathrm{PO}_4^{z7}],\\
c_8 &= [\mathrm{Ca}^{z8}],\\
c_9 &= [\mathrm{Na}^{z9}],\\
c_{10} &= [\mathrm{Cl}^{z10}],
\end{aligned} \tag{68}$$

where $c_1, c_2, \ldots, c_{10}$ represent the molar concentrations of the ionic species involved in the 3D corrosion system, $z_1, z_2, \ldots, z_{10}$ are their respective charge numbers, and ϕ signifies the electrostatic potential, derived from the nonlocal Poisson equation, thus marking the eleventh unknown variable in the system. The reaction terms are directly derived from Eqs. 56 to 67, following the methodology detailed in [69]. As outlined in this reference, the computational domain is segmented into different parts for the computation of reaction terms. For instance, the dissolution of Mg^{2+} ions as per Eq. 56 and the corresponding hydrogen formation from Eq. 57 are calculated at point $\mathbf{x}_i$ within the DCL for a time instance t^{n+1}. The latter is implemented through the reaction term on the hydrogen ion concentration c_2, given by

$$R^{n+1}_{\mathrm{H}_2,i} = \frac{J_{\mathrm{H}_2}}{z_2 F c_{\text{solid}}} \exp\left(-\frac{\alpha_{\mathrm{H}_2} F}{RT}\eta_i^n\right), \qquad \exists \mathbf{x} \in \mathcal{F}_i : \varphi(\mathbf{x}_i, t^n) \neq \varphi(\mathbf{x}, t^n), \tag{69}$$

where J_{H_2} is defined as the proportionality factor at zero overpotential, and α_{H_2} is identified as the charge transfer coefficient. In general, a total of r reactions within the system can be characterized as

$$\sum_{k=1}^{N} p_{k,i} c_k(\mathbf{x}, t) \rightleftharpoons \sum_{k=1}^{N} q_{k,i} c_k(\mathbf{x}, t), \qquad i = 1, 2, \ldots, r, \tag{70}$$

where N denotes the total number of species in the system, while $p_{k,i}$ and $q_{k,i}$ represent the stoichiometric coefficients for the ith reaction. A universal reaction term at a point $\mathbf{x}$ and time t can therefore be written as

$$R_k(\mathbf{x}, t) = \sum_{i=1}^{r} k_{b,i} \left(K_{\mathrm{eq},i} - (q_{k,i} - p_{k,i}) \prod_{n=1}^{N} c_n^{q_{n,i}}(\mathbf{x}, t)\right), \qquad k = 1, 2, \ldots, N, \tag{71}$$

where $k_{b,i}$ is the backward reaction rate for the ith reaction, and $K_{\mathrm{eq},i}$ denotes the corresponding equilibrium constant. It's important to note that the reactions spanning from Eqs. 58 to 67 are considered throughout the entire liquid electrolyte phase as well as within the solid and liquid subdomains of the DCL. Conversely, the dissociation reactions of water, hydrogen carbonate, and hydrogen phosphate are only considered in the liquid phase. The parameters governing these reactions, along with other model parameters for the 3D degradation system, are summarized in the Appendix B, and presented in Table 4.

The constitutive model governing the dissolution of Mg ions into the liquid electrolyte domain is based on a semi-empirical corrosion rate equation initially proposed by [16, 22]. This model has been applied to PD corrosion modeling in the context of bio-degradation for Mg-xGd based bone implant materials, thus naturally extending its application to the NNPP corrosion system. We will now briefly revisit the constitutive assumptions of this model. It postulates that the volume loss of the metallic specimen over time can be accurately described by a semi-empirical two-parameter corrosion rate equation, whereby the volume loss over time is formulated as

$$V_L(t) = \frac{1}{l} \ln\left(1 + \frac{t}{\tau}\right), \tag{72}$$

where $l, \tau > 0$ represent model parameters. From Eq. 72, the volume loss rate can be expressed as

$$\dot{V}_L(t) = \frac{1}{\tau l} \exp\left(-l V_L(t)\right). \tag{73}$$

This latter equation can be related to Faraday’s second law of electrolysis, which correlates the anodic current density with the mass (and consequently, volume) of the dissolving metallic material. Incorporating Eq. 73 into Faraday’s second law yields the anodic current density over time as

$$i_a(t) = \frac{zF\rho}{\tau l M A} \exp\left(-l V_L(t)\right) = \tilde{i}_0 \exp\left(-l V_L(t)\right), \tag{74}$$

where z denotes the metal charge number, ρ is the density, M is the molar mass, and A is the corrosion surface area. The coefficient $\tilde{i}_0$ encapsulates the factors before the exponential and represents the initial anodic current density for an intact metallic specimen. Notably, this relationship mirrors a Tafel-like relation found in electrochemical kinetics, linking volume loss directly to anodic current density rather than overpotential. The parameter l emerges as a critical non-negative model parameter, influencing the degradation layer’s depth and, by extension, moderating the degradation progression as it increases. For this study, l is set as a fixed parameter, as estimated in [27] for corrosion modeling of Mg-10Gd based bone implant screws in physiological conditions. Following the methodology proposed in [13], we posit a linear relationship between the effective solid metal ion flux and diffusivity. Consequently, the diffusion coefficient $D_{1,ij}(t)$ for the Mg ion concentration c_1 across a bond vector $\boldsymbol{\xi} := \mathbf{x}_j - \mathbf{x}_i$ is defined as

$$D_{1,ij}(t) = \begin{cases} D_{1,l}, & \varphi(\mathbf{x}_j, t) = 0 \wedge \varphi(\mathbf{x}_i, t) = 0 \\ D_{1,i} \exp\left(-l V_L(t)\right), & \varphi(\mathbf{x}_j, t) = 1 \oplus \varphi(\mathbf{x}_i, t) = 1 \\ D_{1,s}, & \varphi(\mathbf{x}_j, t) = 1 \wedge \varphi(\mathbf{x}_i, t) = 1 \end{cases}, \tag{75}$$

where $D_{1,l}$, $D_{1,i}$, and $D_{1,s}$ signify the constant diffusion coefficients corresponding to liquid-liquid, interface, and solid-solid interactions, respectively. These coefficients are detailed in Table 4 of Appendix B. The constitutive model for the other species across a bond vector $\boldsymbol{\xi} = \mathbf{x}_j - \mathbf{x}_i$ is defined as

$$D_{k,ij} = \begin{cases} D_{k,l}, & \varphi(\mathbf{x}_j, t) = 0 \wedge \varphi(\mathbf{x}_i, t) = 0 \\ \varepsilon D_{k,l}, & \varphi(\mathbf{x}_j, t) = 1 \oplus \varphi(\mathbf{x}_i, t) = 1 \\ 0, & \varphi(\mathbf{x}_j, t) = 1 \wedge \varphi(\mathbf{x}_i, t) = 1 \end{cases}, \quad k = 2, 3, ..., N, \tag{76}$$

where $N = 10$ represents the total number of species within the system. The diffusion coefficient for interface bonds is denoted as $D_{k,i} := \varepsilon D_{k,l}$, with ε being the ratio of tortuosity to porosity across the DCL. Additionally, the electrical conductivity assumed in the nonlocal

Poisson equation in Eq. 17, is considered constant for this analysis and the equation is exclusively solved in the liquid phase.

7.1 Numerical Simulation Results for 3D Bone Implant Screw

The numerical simulation was conducted over a period of 56 days of simulated immersion in a cylindrical computational domain measuring 3 mm in radius and 5 mm in height. This setup employed a regular grid size of 20 µm, encompassing a total of 4, 393, 605 computational nodes. The simulation adopted a time step size of $\Delta t = 3$ h and a PD horizon of 60 µm. The initial configuration, representing the solid metal phase ($\varphi = 1$) of a M2 × 4 mm headless bone implant screw, is illustrated in Fig. 6, with the surrounding liquid electrolyte phase of SBF ($\varphi = 0$). Detailed initial and boundary conditions for this simulation are compiled in Table 3 within Appendix B.

The simulation was performed on an in-house software developed in C++11, on a computational node within our in-house high-performance computing (HPC) cluster, featuring

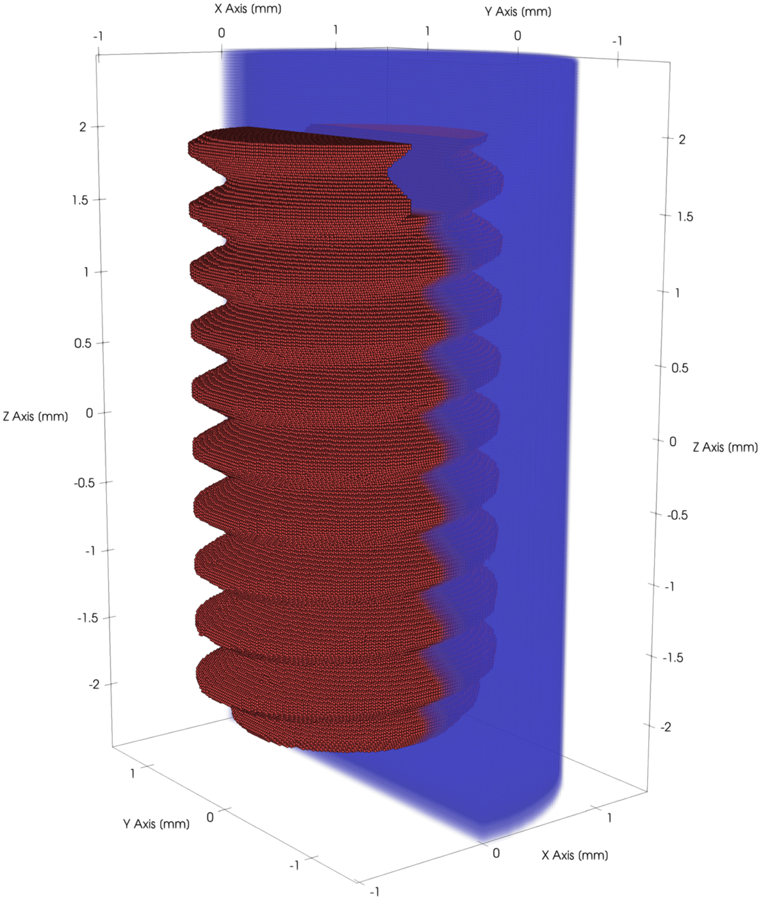

Fig. 6 Topology of the initial solid metallic phase ($\varphi = 1$) represented on a regular grid for the M2 × 4 mm headless bone implant screw, juxtaposed with the cross-sectional cut through the surrounding cylindrical liquid electrolyte phase ($\varphi = 0$) of SBF

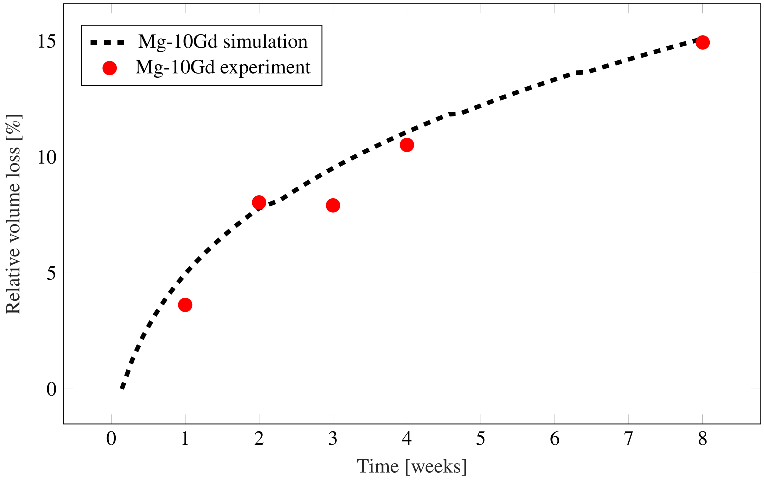

Fig. 7 Simulated and experimental volume loss over time in weight percentage of the Mg-10Gd bone implant screw

dual sockets, each equipped with a 24-core 2.1 GHz Intel Xeon Scalable Platinum 8160 processor, facilitating shared memory multiprocessing parallelism across 48 cores via OpenMP directives. For efficient PD neighborhood search, an efficient spatial hashing algorithm was utilized. The linear systems in Eqs. 38 and 40 were iteratively solved using the Generalized Minimal Residual Method (GMRES), leveraging the functionalities of the standard LAPACK library [3].

Figure 7 depicts the progression of corrosion through the macroscopic volume loss over time for the bone implant screw with experimental mean values for volume loss of Mg-10Gd based implant screws, indicating a strong correlation between the simulated and experimental data over an 8-week immersion period. As previously noted in Section 6.1 with respect to the 1D pencil electrode corrosion scenario, experimental data for species distribution, par-

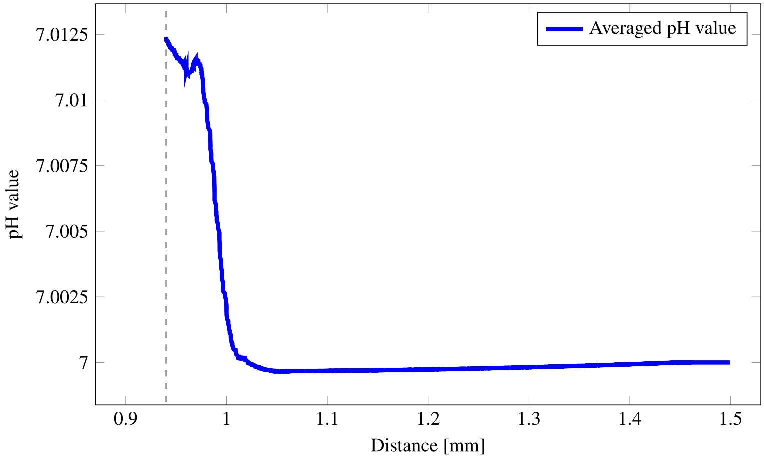

Fig. 8 Average pH value in the electrolyte starting from the surface of the screw (at the screw radius) and at a height of $z = 0$ within the liquid phase, with the boundary between the solid and liquid phases marked by a dashed vertical line

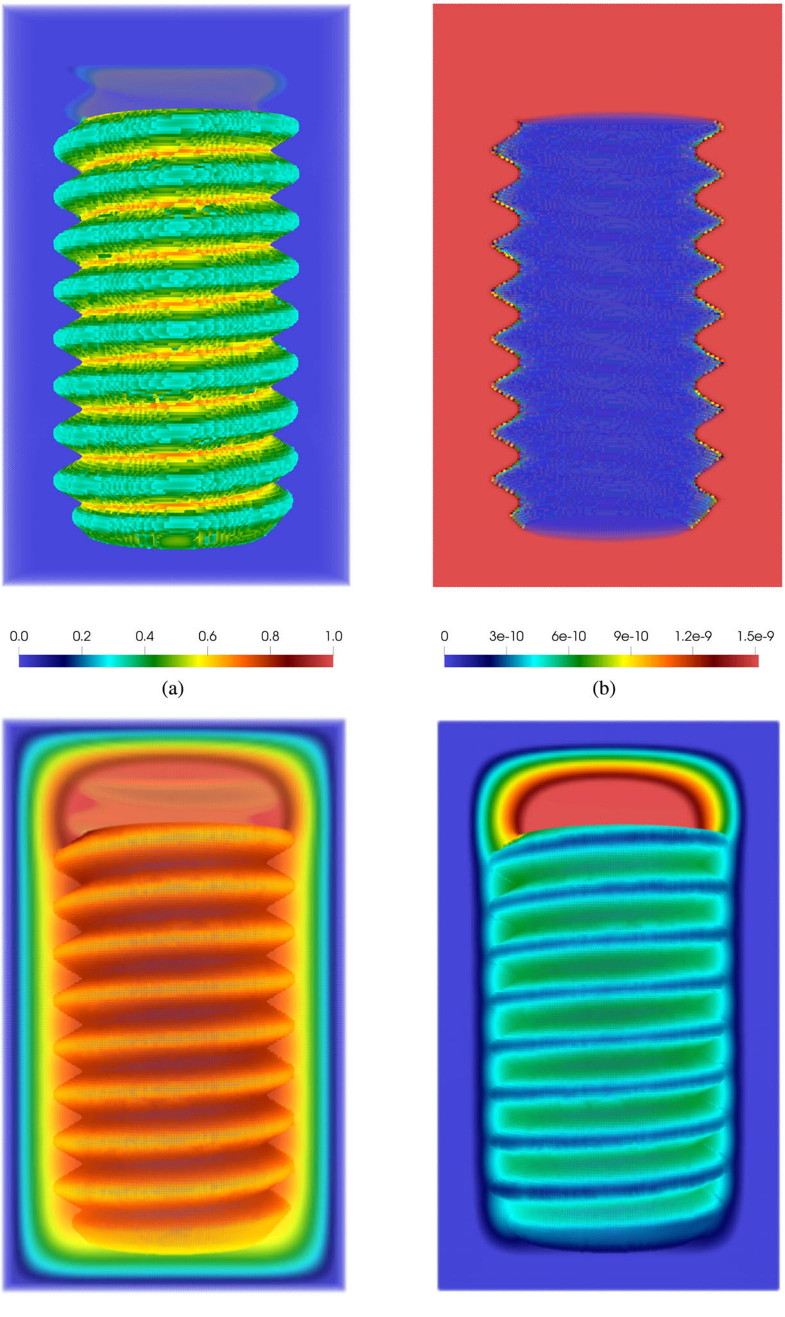

(a) (b)

(c) (d)

Fig. 9 Normalized concentration distributions in the domain of various ionic species at the final time instance after 8 weeks of simulated immersion in SBF: (a) magnesium, (b) hydrogen ions, (c) carbonate, (d) phosphate ticularly in the context of *in vitro* corrosion of Mg-based implants, are scarce. Therefore, the results presented herein aim to provide a qualitative analysis. Figure 9 decpits the normalized concentration distributions of Mg ions, hydrogen ions, carbonate, and phosphate within the computational domain at the final time instance of 8 weeks of simulated immersion. All concentration values are normalized against $c_{\text{solid}} = 66082.4\text{mol}/\text{m}^3$, which represents the initial concentration of Mg-10Gd in the intact metal phase, thereby scaling the maximum Mg ion concentration to 1. Notably, the corrosion progresses most rapidly along the screw threads, illustrated by reduced Mg concentration values in Fig. 9a. This observation aligns with the assumption of a homogeneous corrosion profile, characterized by uniform diffusion coefficients for each bond vector $\boldsymbol{\xi} = \mathbf{x}_j - \mathbf{x}_i$, and the respective phase conditions of the endpoints at all times. Consequently, no formation of increased localization and irregular pitting corrosion is considered, which aligns with findings from the respective literature [38]. Given the slow progression of *in vitro* corrosion, the concentrations of other components stabilize rapidly and are omitted here for succinctness. Notably, Fig. 9d showcases an accumulation of phosphate within the screw slot, suggesting a concentration higher within this confined region than in the surrounding liquid, which is also partially observed for carbonate distribution in Fig. 9c.

To further evaluate the numerical findings, the averaged pH value across the radius of the cylindrical screw, extending from the solid-liquid corrosion interface, is presented in Fig. 8. Qualitatively, the increase in pH value across the screw radius, as seen in Fig. 8, and a reduction of hydrogen ions, as shown in Fig. 9b, correspond with experimental results documented in [69]. Nevertheless, the pH value increases provided in [69] are slightly greater than those found in our numerical study. The discrepancy could be attributed due to both the experiments being limited to only 28 days of immersion in SBF as well as the use of pure Mg as the corrosion sample, unlike the Mg-10Gd alloy investigated in our study. Furthermore, the model parameters outlined in Table 4, based on literature values and approximations to be in line with macroscopic volume loss data, might need to be adjusted to the particular corrosion system under study, as proposed by [27]. Moreover, the choice of boundary conditions and the size of the computational domain significantly influence the numerical results, thus a larger computational domain with a bigger portion of the surrounding liquid electrolyte may mitigate the differences to experimental obersationvs. However, it is should be noted that, 3D NNPP simulations on HPC platforms are still characterized by high computational demands, for example, simulating 56 days of immersion requires approximately 21 days of computation on 48 parallel threads using OpenMP. Thus, the future research will be concentrated on the creation of the more effective numerical solution methods.

8 Conclusions

In this paper, we derived the nonlocal Nernst-Planck-Poisson (NNPP) system of equations and demonstrated their convergence with the classical local counterparts in the limit of vanishing nonlocal interactions. We defined an effective diffusive corrosion layer across which material properties change, and where mass transfer of metal ions into the liquid electrolyte occurs. At this layer, constitutive models for the NNPP system based on diffusion-electromigration-reaction, grounded in the electrochemical description of a given corrosion system, were established, providing a general framework for constitutive peridynamic corrosion modeling. We introduced a straightforward and easy-to-implement numerical scheme, utilizing semi-implicit time discretization and the standard meshfree approach of peridynamics on a regular grid to solve the $N + 1$ linear systems of NNPP equations using a Newton-Raphson scheme.

Although the general applicability toward 3D corrosion models remains computationally expensive, it is identified as an area for future research to develop more efficient solution techniques. The performance and accuracy of the NNPP system for peridynamic corrosion modeling were validated through numerical examples. In a 1D example of pencil electrode corrosion, we observed very good agreement with experimental corrosion length data and qualitatively good agreement with results obtained from phase-field corrosion models. In the 3D numerical example, we demonstrated the applicability of the NNPP system for modeling the complex electrochemical system of in vitro degradation of an Mg-10Gd based headless bone implant screw in simulated body fluid, achieving good agreement with experimentally obtained macroscopic volume loss data and qualitatively observing an increase in pH value across the corrosion surface, aligning with experimental findings. Future studies will aim to establish the effectiveness of the proposed system toward general corrosion phenomena.

Appendix A Model parameters for 1D Example

Table 1 Initial and Boundary Condition for 1D Pencil Electrode Corrosion

Species	Initial Value in Solid ($\varphi = 1$)	Initial Value in Liquid ($\varphi = 0$)	Boundary Condition ($x = 0\,\mu\text{m}$)	Boundary Condition ($x = 200\,\mu\text{m}$)
c_1	1	0	1	0
c_2	0	10^{-9}	0	0
c_3	0	$1/143.1$	0	$1/143.1$
c_4	0	$1/143.1$	0	$1/143.1$
c_5	0	$10^{-7}/143.1$	0	$10^{-7}/143.1$
c_6	0	$10^{-7}/143.1$	0	$10^{-7}/143.1$
ϕ	0	0	–	0

Table 2 Simulation and Model Parameters for 1D Pencil Electrode Corrosion

Symbol	Value	Unit	Description
T	298.15	K	Temperature
G	8.3145	$\text{J}\,\text{mol}^{-1}\,\text{K}^{-1}$	Gas constant
F	96485	$\text{C}\,\text{mol}^{-1}$	Faraday's constant
δ	1.25	µm	Horizon
z_1	2.19	–	Charge number on species c_1
z_2	1.19	–	Charge number on species c_2
z_3	-1	–	Charge number on species c_3
z_4	1	–	Charge number on species c_4
z_5	1	–	Charge number on species c_5
z_6	-1	–	Charge number on species c_6
c_{solid}	143.1	$\text{mol}\,\text{L}^{-1}$	Concentration of intact metal material
c_{sat}	5.1	$\text{mol}\,\text{L}^{-1}$	Saturation concentration of metal ions in electrolyte
$D_{1,l}$	9.75×10^{-10}	m^2/s	Diffusion coefficient of species c_1 for liquid-liquid bonds
$D_{1,i}$	2.125×10^{-12}	m^2/s	Diffusion coefficient of species c_1 for interface bonds
$D_{1,s}$	2.125×10^{-12}	m^2/s	Diffusion coefficient of species c_1 for solid-solid bonds

Table 2 continued

Symbol	Value	Unit	Description
$D_{2,l}$	4.25×10^{-10}	m^2/s	Diffusion coefficient of species c_2 for liquid-liquid bonds
$D_{2,i}$	8.5×10^{-13}	m^2/s	Diffusion coefficient of species c_2 for interface bonds
$D_{2,s}$	-	-	Diffusion coefficient of species c_2 for solid-solid bonds
$D_{3,l}$	8.5×10^{-11}	m^2/s	Diffusion coefficient of species c_3 for liquid-liquid bonds
$D_{3,i}$	8.5×10^{-12}	m^2/s	Diffusion coefficient of species c_3 for interface bonds
$D_{3,s}$	–	–	Diffusion coefficient of species c_3 for solid-solid bonds
$D_{4,l}$	8.5×10^{-11}	m^2/s	Diffusion coefficient of species c_4 for liquid-liquid bonds
$D_{4,i}$	8.5×10^{-12}	m^2/s	Diffusion coefficient of species c_4 for interface bonds
$D_{4,s}$	–	–	Diffusion coefficient of species c_4 for solid-solid bonds
$D_{5,l}$	4.25×10^{-10}	m^2/s	Diffusion coefficient of species c_5 for liquid-liquid bonds
$D_{5,i}$	8.5×10^{-12}	m^2/s	Diffusion coefficient of species c_5 for interface bonds
$D_{5,s}$	–	–	Diffusion coefficient of species c_5 for solid-solid bonds
$D_{6,l}$	1.7×10^{-10}	m^2/s	Diffusion coefficient of species c_6 for liquid-liquid bonds
$D_{6,i}$	8.5×10^{-12}	m^2/s	Diffusion coefficient of species c_6 for interface bonds
$D_{6,s}$	–	–	Diffusion coefficient of species c_6 for solid-solid bonds
ϕ_{applied}	-300	mV	Applied metal potential (SHE)
ϕ_0	-477	mV	Standard electrode potential (SHE)
ϵ	6.1×10^6	Sm^{-1}	Electrical conductivity in the liquid electrolyte phase
$k_{f,1}$	5×10^{-9}	s^{-1}	Forward reaction rate in Eq. 47
$k_{b,1}$	0.0158	$mol^{-1}\,s^{-1}$	Backward reaction rate in Eq. 47
$k_{f,2}$	2.5×10^{-8}	$mol\,s^{-1}$	Forward reaction rate in Eq. 48
$k_{b,2}$	2.5×10^{-16}	$mol^{-1}\,s^{-1}$	Backward reaction rate in Eq. 48
J_{50}	-2×10^{-3}	$A\,m\,mol^{-1}$	Pre-exponential coefficient in Eq. 52
J_{60}	8×10^{-10}	A/m^2	Pre-exponential coefficient in Eq. 53

Appendix B Model parameters for 3D Example

Table 3 Initial and Boundary Condition for 3D Bone Implant Screw Degradation

Species	Initial Value in Solid ($\varphi = 1$)	Initial Value in Liquid ($\varphi = 0$)	Boundary Condition
c_1	1	0	0
c_2	0	$10^{-4}/66082.4$	$10^{-4}/66082.4$
c_3	0	$10^{-4}/66082.4$	$10^{-4}/66082.4$
c_4	0	$34.88/66082.4$	$34.88/66082.4$
c_5	0	0	0
c_6	0	$1.39/66082.4$	$1.39/66082.4$
c_7	0	0	0
c_8	0	$2.31/66082.4$	$2.31/66082.4$
c_9	0	$142/66082.4$	$142/66082.4$
c_{10}	0	$109.9/66082.4$	$109.9/66082.4$
ϕ	0	0	0

Table 4 Simulation and Model Parameters for 3D Bone Implant Screw Degradation

Symbol	Value	Unit	Description
T	298.15	K	Temperature
G	8.3145	$\mathrm{J\,mol^{-1}\,K^{-1}}$	Gas constant
F	96485	$\mathrm{C\,mol^{-1}}$	Faraday's constant
δ	60	μm	Horizon
z_1	2	–	Charge number on species c_1
z_2	1	–	Charge number on species c_2
z_3	-1	–	Charge number on species c_3
z_4	-1	–	Charge number on species c_4
z_5	-2	–	Charge number on species c_5
z_6	-2	–	Charge number on species c_6
z_7	-3	–	Charge number on species c_7
z_8	2	–	Charge number on species c_8
z_9	1	–	Charge number on species c_9
z_{10}	-1	–	Charge number on species c_{10}
ε	10^{-3}	–	Tortuosity to porosity ratio of the DCL
l	11.0524	$\mathrm{m^{-3}}$	Volume proportionality factor (*cf.* Eq. 75)
c_{solid}	66082.4	$\mathrm{mol/m^3}$	Concentration of intact Mg-10Gd material
c_{sat}	2312.88	$\mathrm{mol/m^3}$	Saturation concentration of Mg-10Gd ions in electrolyte
$D_{1,l}$	7.1×10^{-10}	$\mathrm{m^2/s}$	Diffusion coefficient of species c_1 for liquid-liquid bonds
$D_{1,i}$	1×10^{-15}	$\mathrm{m^2/s}$	Diffusion coefficient of species c_1 for interface bonds
$D_{1,s}$	2.125×10^{-17}	$\mathrm{m^2/s}$	Diffusion coefficient of species c_1 for solid-solid bonds
$D_{2,l}$	9.31×10^{-9}	$\mathrm{m^2/s}$	Diffusion coefficient of species c_2 for liquid-liquid bonds
$D_{2,i}$	9.31×10^{-13}	$\mathrm{m^2/s}$	Diffusion coefficient of species c_2 for interface bonds
$D_{2,s}$	–	–	Diffusion coefficient of species c_2 for solid-solid bonds
$D_{3,l}$	5.27×10^{-9}	$\mathrm{m^2/s}$	Diffusion coefficient of species c_3 for liquid-liquid bonds
$D_{3,i}$	5.27×10^{-12}	$\mathrm{m^2/s}$	Diffusion coefficient of species c_3 for interface bonds
$D_{3,s}$	–	–	Diffusion coefficient of species c_3 for solid-solid bonds
$D_{4,l}$	1.19×10^{-9}	$\mathrm{m^2/s}$	Diffusion coefficient of species c_4 for liquid-liquid bonds
$D_{4,i}$	1.19×10^{-12}	$\mathrm{m^2/s}$	Diffusion coefficient of species c_4 for interface bonds
$D_{4,s}$	–	–	Diffusion coefficient of species c_4 for solid-solid bonds
$D_{5,l}$	9.23×10^{-10}	$\mathrm{m^2/s}$	Diffusion coefficient of species c_5 for liquid-liquid bonds
$D_{5,i}$	9.23×10^{-13}	$\mathrm{m^2/s}$	Diffusion coefficient of species c_5 for interface bonds
$D_{5,s}$	–	–	Diffusion coefficient of species c_5 for solid-solid bonds
$D_{6,l}$	6.9×10^{-10}	$\mathrm{m^2/s}$	Diffusion coefficient of species c_6 for liquid-liquid bonds
$D_{6,i}$	6.9×10^{-13}	$\mathrm{m^2/s}$	Diffusion coefficient of species c_6 for interface bonds
$D_{6,s}$	–	–	Diffusion coefficient of species c_6 for solid-solid bonds
$D_{7,l}$	6.12×10^{-10}	$\mathrm{m^2/s}$	Diffusion coefficient of species c_7 for liquid-liquid bonds
$D_{7,i}$	6.12×10^{-13}	$\mathrm{m^2/s}$	Diffusion coefficient of species c_7 for interface bonds
$D_{7,s}$	–	–	Diffusion coefficient of species c_7 for solid-solid bonds
$D_{8,l}$	7.93×10^{-10}	$\mathrm{m^2/s}$	Diffusion coefficient of species c_8 for liquid-liquid bonds

Table 4 continued

Symbol	Value	Unit	Description
$D_{8,i}$	7.93×10^{-13}	m^2/s	Diffusion coefficient of species c_8 for interface bonds
$D_{8,s}$	–	–	Diffusion coefficient of species c_8 for solid-solid bonds
$D_{9,l}$	1.33×10^{-9}	m^2/s	Diffusion coefficient of species c_9 for liquid-liquid bonds
$D_{9,i}$	1.33×10^{-12}	m^2/s	Diffusion coefficient of species c_9 for interface bonds
$D_{9,s}$	–	–	Diffusion coefficient of species c_9 for solid-solid bonds
$D_{10,l}$	2.03×10^{-9}	m^2/s	Diffusion coefficient of species c_{10} for liquid-liquid bonds
$D_{10,i}$	2.03×10^{-12}	m^2/s	Diffusion coefficient of species c_{10} for interface bonds
$D_{10,s}$	–	–	Diffusion coefficient of species c_{10} for solid-solid bonds
ϵ	6.1×10^6	$\mathrm{S\,m}^{-1}$	Electrical conductivity in the liquid electrolyte medium
$\mathrm{pK}_{\mathrm{brucite}}$	15.97	–	Precipitation constant of brucite (*cf.* Eq. 58)
$\mathrm{pK}_{\mathrm{magnesite}}$	4.73	–	Precipitation constant of magnesite (*cf.* Eq. 59)
$\mathrm{pK}_{\mathrm{nesquehonite}}$	-4.49	–	Precipitation constant of nesquehonite (*cf.* Eq. 60)
$\mathrm{pK}_{\mathrm{bobierrite}}$	-2.98	–	Precipitation constant of bobierrite (*cf.* Eq. 61)
$\mathrm{pK}_{\mathrm{calcite}}$	-1.8	–	Precipitation constant of calcite (*cf.* Eq. 63)
$\mathrm{pK}_{\mathrm{hydroxyapatite}}$	-35.42	–	Precipitation constant of hydroxyapatite (*cf.* Eq. 64)
$\mathrm{pK}_{\mathrm{water}}$	13.61	–	Dissociation constant of water (*cf.* Eq. 65)
$\mathrm{pK}_{\mathrm{carbonate}}$	10.24	–	Dissociation constant of hydrogen carbonate (*cf.* Eq. 66)
$\mathrm{pK}_{\mathrm{phosphate}}$	10.24	–	Dissociation constant of hydrogen phosphate (*cf.* Eq. 67)
J_{H_2}	-2×10^{-3}	$\mathrm{A\,m\,mol}^{-1}$	Pre-exponential coefficient in Eq. 69
$k_{b,1}$	9.0245×10^{-21}	$\mathrm{m}^7/\mathrm{mol}^2\mathrm{s}$	Backward reaction rate (*cf.* Eq. 58)
$k_{b,2}$	7.0332×10^{-9}	$\mathrm{m}^7/\mathrm{mol}^2\mathrm{s}$	Backward reaction rate (*cf.* Eq. 59)
$k_{b,3}$	7.0023×10^{-10}	$\mathrm{m}^7/\mathrm{mol}^2\mathrm{s}$	Backward reaction rate (*cf.* Eq. 60)
$k_{b,4}$	1.0798×10^{-2}	$\mathrm{m}^7/\mathrm{mol}^2\mathrm{s}$	Backward reaction rate (*cf.* Eq. 61)
$k_{b,5}$	8.0037×10^{-24}	$\mathrm{m}^7/\mathrm{mol}^2\mathrm{s}$	Backward reaction rate (*cf.* Eq. 63)
$k_{b,6}$	9.001×10^{-16}	$\mathrm{m}^7/\mathrm{mol}^2\mathrm{s}$	Backward reaction rate (*cf.* Eq. 64)
$k_{b,7}$	1.4×10^2	$\mathrm{m}^3/\mathrm{mol/s}$	Backward reaction rate (*cf.* Eq. 65)
$k_{b,8}$	1.4×10^2	$\mathrm{m}^3/\mathrm{mol/s}$	Backward reaction rate (*cf.* Eq. 66)
$k_{b,9}$	1.4×10^2	$\mathrm{m}^3/\mathrm{mol/s}$	Backward reaction rate (*cf.* Eq. 67)

Acknowledgements Funded by the Deutsche Forschungsgemeinschaft (DFG, German Research Foundation) - 470246804.

Author Contributions A.H. and A.S. conceptualized the study. Formal analysis was performed by A.H. and A.S. Funding acquisition was managed by C.C. The investigation was conducted by A.H., A.S., D.H., and F.B. Methodology was developed by A.H., A.S., D.H. and F.B. Project administration was handled by C.C. Resources were provided by C.C. Software development was undertaken by A.H. and A.S. C.C. supervised the project. Validation was conducted by D.H., S.J., and F.B. Visualization was carried out by A.H. and A.S. A.H. and A.S. wrote the original draft of the manuscript. D.H., S.J., F.B., and C.C. reviewed and edited the manuscript. All authors reviewed and approved the final manuscript.

Funding Open Access funding enabled and organized by Projekt DEAL. The research was supported by Deutsche Forschungsgemeinschaft (DFG, German Research Foundation) - 470246804

Data Availability No datasets were generated or analysed during the current study.

Declarations

The authors declare that they have no conflict of interest to disclose.

Competing interests The authors declare no competing interests.

References

1. Al Baraghtheh T, Hermann A, Shojaei A, Willumeit-Römer R, Cyron CJ, Zeller-Plumhoff B (2023) Utilizing computational modelling to bridge the gap between in vivo and in vitro degradation rates for mg-xgd implants. Corros Mater Degrad 4(2):274–283
2. Amukarimi S, Mozafari M (2021) Biodegradable magnesium-based biomaterials: An overview of challenges and opportunities. MedComm 2(2):123–144
3. Anderson E, Bai Z, Bischof C, Blackford LS, Demmel J, Dongarra J, Du Croz J, Greenbaum A, Hammarling S, McKenney A, et al (1999) LAPACK users' guide. SIAM
4. Anicode SV, Madenci E, Phan N (2023) A unified method to simulate electrodeposition and galvanic corrosion using the peridynamic differential operator. Comput Methods Appl Mech Eng 408:115968
5. Ansari TQ, Huang H, Shi SQ (2021) Phase field modeling for the morphological and microstructural evolution of metallic materials under environmental attack. npj Comput Mater 7(1):143
6. Ansari TQ, Luo JL, Shi SQ (2019) Modeling the effect of insoluble corrosion products on pitting corrosion kinetics of metals. NPJ Mater Degrad 3(1):28
7. Ansari TQ, Xiao Z, Hu S, Li Y, Luo JL, Shi SQ (2018) Phase-field model of pitting corrosion kinetics in metallic materials. npj Comput Mater 4(1):38
8. Bie Y, Ren H, Rabczuk T, Bui TQ, Wei Y (2024) The fully coupled thermo-mechanical dual-horizon peridynamic correspondence damage model for homogeneous and heterogeneous materials. Comput Methods Appl Mech Eng 420:116730
9. Bobaru F, Duangpanya M (2010) The peridynamic formulation for transient heat conduction. Int J Heat Mass Transfer 53(19–20):4047–4059
10. Bobaru F, Duangpanya M (2012) A peridynamic formulation for transient heat conduction in bodies with evolving discontinuities. J Comput Phys 231(7):2764–2785
11. Bobaru F, Foster JT, Geubelle PH, Silling SA (2016) Handbook of peridynamic modeling, CRC Press
12. Boland EL, Grogan JA, McHugh PE (2017) Computational modeling of the mechanical performance of a magnesium stent undergoing uniform and pitting corrosion in a remodeling artery. J Med Devices 11(2):021013
13. Chen Z, Bobaru F (2015) Peridynamic modeling of pitting corrosion damage. J Mech Phys Solids 78:352–381
14. Chen Z, Bobaru F (2015) Selecting the kernel in a peridynamic formulation: A study for transient heat diffusion. Comput Phys Commun 197:51–60
15. Chen Z, Jafarzadeh S, Zhao J, Bobaru F (2021) A coupled mechano-chemical peridynamic model for pit-to-crack transition in stress-corrosion cracking. J Mech Phys Solids 146:104203
16. Dahms M, Höche D, Ahmad Agha N, Feyerabend F, Willumeit-Römer R (2018) A simple model for long-time degradation of magnesium under physiological conditions. Mater Corros 69(2):191–196
17. Diehl P, Prudhomme S, Lévesque M (2019) A review of benchmark experiments for the validation of peridynamics models. J Peridynamics Nonlocal Model 1:14–35
18. Ernst P, Newman RC (2002) Pit growth studies in stainless steel foils. i. introduction and pit growth kinetics. Corros Sci 44(5):927–941
19. Ernst P, Newman RC (2002) Pit growth studies in stainless steel foils. ii. effect of temperature, chloride concentration and sulphate addition. Corros Sci 44(5):943–954
20. Fuhrmann J (2015) Comparison and numerical treatment of generalised nernst-planck models. Comput Phys Commun 196:166–178

21. Gartzke AK, Julmi S, Klose C, Waselau AC, Meyer-Lindenberg A, Maier HJ, Besdo S, Wriggers P (2020) A simulation model for the degradation of magnesium-based bone implants. J Mech Behav Biomed Mater 101:103411
22. Gießgen T, Mittelbach A, Höche D, Zheludkevich M, Kainer KU (2019) Enhanced predictive corrosion modeling with implicit corrosion products. Mater Corros 70(12):2247–2255
23. Gonzalez J, Hou RQ, Nidadavolu EP, Willumeit-Römer R, Feyerabend F (2018) Magnesium degradation under physiological conditions-best practice. Bioact Mater 3(2):174–185
24. Grogan JA, O'brien BJ, Leen SB, McHugh PE (2011) A corrosion model for bioabsorbable metallic stents. Acta Biomater 7(9):3523–3533
25. Höche D, Isakovic J (2012) Level-set modeling of galvanic corrosion of magnesium. In: International Conference on Magnesium Alloys and Their Applications, 9, Vancouver, p 325–331
26. Hermann A, Shojaei A, Seleson P, Cyron CJ, Silling SA (2023) Dirichlet-type absorbing boundary conditions for peridynamic scalar waves in two-dimensional viscous media. Int J Numer Methods Eng 124(16):3524–3553
27. Hermann A, Shojaei A, Steglich D, Höche D, Zeller-Plumhoff B, Cyron CJ (2022) Combining peridynamic and finite element simulations to capture the corrosion of degradable bone implants and to predict their residual strength. Int J Mech Sci 220:107143
28. Imran R, Al Rashid A, Koç M (2022) Review on computational modeling for the property, process, product and performance (pppp) characteristics of additively manufactured porous magnesium implants. Bioprinting 28:e00236
29. Jafarzadeh S, Chen Z, Bobaru F (2018) Peridynamic modeling of intergranular corrosion damage. J Electrochem Soc 165(7):C362
30. Jafarzadeh S, Chen Z, Bobaru F (2018) Peridynamic modeling of repassivation in pitting corrosion of stainless steel. Corrosion 74(4):393–414
31. Jafarzadeh S, Chen Z, Bobaru F (2019) Computational modeling of pitting corrosion. Corros Rev 37(5):419–439
32. Jafarzadeh S, Chen Z, Li S, Bobaru F (2019) A peridynamic mechano-chemical damage model for stress-assisted corrosion. Electrochimica Acta 323:134795
33. Jafarzadeh S, Chen Z, Zhao J, Bobaru F (2019) Pitting, lacy covers, and pit merger in stainless steel: 3d peridynamic models. Corros Sci 150:17–31
34. Jafarzadeh S, Silling S, Liu N, Zhang Z, Yu Y (2024) Peridynamic neural operators: A data-driven nonlocal constitutive model for complex material responses. arXiv:2401.06070
35. Kandekar C, Ravikumar A, Höche D, Weber WE (2023) A partitioned computational framework for damage evolution in stress corrosion cracking utilizing phase-field. PAMM 22(1):e202200211
36. Kieke M, Feyerabend F, Lemaitre J, Behrens P, Willumeit-Römer R (2016) Degradation rates and products of pure magnesium exposed to different aqueous media under physiological conditions. BioNanoMaterials 17(3–4):131–143
37. Kovacevic S, Ali W, Martínez-Pañeda E, LLorca J (2023) Phase-field modeling of pitting and mechanically-assisted corrosion of mg alloys for biomedical applications. Acta Biomaterialia 164:641–658
38. Krüger D, Galli S, Zeller-Plumhoff B, Wieland DF, Peruzzi N, Wiese B, Heuser P, Moosmann J, Wennerberg A, Willumeit-Römer R (2022) High-resolution ex vivo analysis of the degradation and osseointegration of mg-xgd implant screws in 3d. Bioact Mater 13:37–52
39. Lees E, Rokkam S, Shanbhag S, Gunzburger M (2017) The electroneutrality constraint in nonlocal models. J Chem Phys 147(12)
40. Li Z, Huang D, Ren H, Rabczuk T (2023) Weak form of bond-associated peridynamic differential operator for solving differential equations. Eng Comput 39(5):3491–3507
41. Liu H, Chen Z (2024) On the one-point quadrature discretization in peridynamics: A novel perspective from monte carlo integration. Comput Phys Commun 298:109115
42. Luthringer BJ, Feyerabend F, Willumeit-Römer R (2014) Magnesium-based implants: a mini-review. Magnesium Res 27(4):142–154
43. Ma S, Zhang D, Markert B (2019) Phase field modelling of stress assisted corrosion of biodegradable magnesium alloys. PAMM 19(1):e201900442
44. Ma S, Zhou B, Markert B (2018) Numerical simulation of the tissue differentiation and corrosion process of biodegradable magnesium implants during bone fracture healing. ZAMM-J Appl Math Mech/Zeitschrift für Angewandte Mathematik und Mechanik 98(12):2223–2238
45. Madenci E, Barut A, Futch M (2016) Peridynamic differential operator and its applications. Comput Methods Appl Mech Eng 304:408–451
46. Mai W, Soghrati S (2018) New phase field model for simulating galvanic and pitting corrosion processes. Electrochimica Acta 260:290–304

47. Mai W, Soghrati S, Buchheit RG (2016) A phase field model for simulating the pitting corrosion. Corros Sci 110:157–166
48. Martinez DC, Dobkowska A, Marek R, Ćwieka H, Jaroszewicz J, Płociński T, Donik Č, Helmholz H, Luthringer-Feyerabend B, Zeller-Plumhoff B et al (2023) In vitro and in vivo degradation behavior of mg-0.45 zn-0.45 ca (zx00) screws for orthopedic applications. Bioact Mater 28:132–154
49. Negrescu AM, Necula MG, Costache M (2020) In vitro and in vivo biological performance of mg-based bone implants. Rev Biol Biomed Sci 3:11–41
50. Ni T, Fan X, Zhang J, Zaccariotto M, Galvanetto U, Schrefler BA (2023) A peridynamic-enhanced finite element method for thermo-hydro-mechanical coupled problems in saturated porous media involving cracks. Comput Methods Appl Mech Eng 417:116376
51. Ongaro G, Shojaei A, Mossaiby F, Hermann A, Cyron CJ, Trovalusci P (2023) Multi-adaptive spatial discretization of bond-based peridynamics. Int J Fract 244(1):1–24
52. Oterkus S, Madenci E, Agwai A (2014) Peridynamic thermal diffusion. J Comput Phys 265:71–96
53. Pidaparti RM, Fang L, Palakal MJ (2008) Computational simulation of multi-pit corrosion process in materials. Comput Mater Sci 41(3):255–265
54. Pirzadeh A, Dalla Barba F, Bobaru F, Sanavia L, Zaccariotto M, Galvanetto U (2024) Elastoplastic peridynamic formulation for materials with isotropic and kinematic hardening. Eng Comput
55. Preve D, Lenarda P, Bianchi D, Gizzi A (2024) Phase field modelling and simulation of damage occurring in human vertebra after screws fixation procedure. Comput Mech 1–20
56. Sanchez AH, Luthringer BJ, Feyerabend F, Willumeit R (2015) Mg and mg alloys: how comparable are in vitro and in vivo corrosion rates? a review. Acta Biomaterialia 13:16–31
57. Seleson P, Ha YD, Beneddine S (2015) Concurrent coupling of bond-based peridynamics and the navier equation of classical elasticity by blending. Int J Multiscale Comput Eng 13(2):1
58. Seleson P, Parks M (2011) On the role of the influence function in the peridynamic theory. Int J Multiscale Comput Eng 9(6)
59. Seleson P, Pasetto M, John Y, Trageser J, Reeve ST (2024) Pdmatlab2d: A peridynamics matlab two-dimensional code. J Peridynamics Nonlocal Model 6(1):149–205
60. Shojaei A, Galvanetto U, Rabczuk T, Jenabi A, Zaccariotto M (2019) A generalized finite difference method based on the peridynamic differential operator for the solution of problems in bounded and unbounded domains. Comput Methods Appl Mech Eng 343:100–126
61. Shojaei A, Hermann A, Seleson P, Cyron CJ (2020) Dirichlet absorbing boundary conditions for classical and peridynamic diffusion-type models. Comput Mech 66:773–793
62. Silling SA (2000) Reformulation of elasticity theory for discontinuities and long-range forces. J Mech Phys Solids 48(1):175–209
63. Silling SA, Lehoucq RB (2010) Peridynamic theory of solid mechanics. Adv Appl Mech 44:73–168
64. Steglich D, Besson J, Reinke I, Helmholz H, Luczak M, Garamus VM, Wiese B, Höche D, Cyron CJ, Willumeit-Römer R (2023) Strength and ductility loss of magnesium-gadolinium due to corrosion in physiological environment: Experiments and modeling. J Mech Behav Biomed Mater 144:105939
65. Tian C, Fan S, Juan D, Zhou Z, Chen Z, Bobaru F (2023) A peridynamic model for advection-reaction-diffusion problems. Comput Methods Appl Mech Eng 415:116206
66. Wang J, Wei H, Zhang X, Pan W (2019) Modeling heat transfer subject to inhomogeneous neumann boundary conditions by smoothed particle hydrodynamics and peridynamics. Int J Heat Mass Transfer 139:948–962
67. Wang X, Wang B, Meyerson M, Mullins CB, Fu Y, Zhu L, Chen L (2018) A phase-field model integrating reaction-diffusion kinetics and elasto-plastic deformation with application to lithiated selenium-doped germanium electrodes. Int J Mech Sci 144:158–171
68. Willumeit-Römer R, Bruns S, Helmholz H, Krüger D, Wiese B, Galli S, Moosmann J, Zeller-Plumhoff B (2022) The comparability of in vitro and in vivo experiments for degradable mg implants. In: Magnesium Technology 2022, p 9–16. Springer
69. Zeller-Plumhoff B, AlBaraghtheh T, Höche D, Willumeit-Römer R (2022) Computational modelling of magnesium degradation in simulated body fluid under physiological conditions. J Magnes Alloy 10(4):965–978
70. Zeller-Plumhoff B, Laipple D, Slominska H, Iskhakova K, Longo E, Hermann A, Flenner S, Greving I, Storm M, Willumeit-Römer R (2021) Evaluating the morphology of the degradation layer of pure magnesium via 3d imaging at resolutions below 40 nm. Bioact Mater 6(12):4368–4376
71. Zhao J, Chen Z, Mehrmashhadi J, Bobaru F (2018) Construction of a peridynamic model for transient advection-diffusion problems. Int J Heat Mass Transfer 126:1253–1266
72. Zhao J, Jafarzadeh S, Chen Z, Bobaru F (2024) Enforcing local boundary conditions in peridynamic models of diffusion with singularities and on arbitrary domains. Eng Comput

73. Zhao J, Jafarzadeh S, Rahmani M, Chen Z, Kim Y-R, Bobaru F (2021) A peridynamic model for galvanic corrosion and fracture. Electrochimica Acta 391:138968